frontiers | Frontiers in Earth Science

TYPE Original Research
PUBLISHED 02 September 2022
DOI 10.3389/feart.2022.873785

OPEN ACCESS

EDITED BY
Christian Creixell,
Servicio Nacional de Geología y Minería de Chile, Chile

REVIEWED BY
Samuel Angiboust,
Université de Lyon, France
Sebastian Oriolo,
Consejo Nacional de Investigaciones Científicas y Técnicas, Argentina

*CORRESPONDENCE
J. Bastías,
j.bastias.silva@gmail.com

SPECIALTY SECTION
This article was submitted to Structural Geology and Tectonics, a section of the journal Frontiers in Earth Science

RECEIVED 11 February 2022
ACCEPTED 07 July 2022
PUBLISHED 02 September 2022

CITATION
Palape C, Quezada P, Bastías J, Hervé F, Reyes T, Veas M, Vildoso F, Calderón M, Theye T, Fuentes F and Chiaradia M (2022), Forearc tectonics and volcanism during the Devonian–Carboniferous evolution of the North Patagonian segment, southern Chile (41,3°S). *Front. Earth Sci.* 10:873785. doi: 10.3389/feart.2022.873785

Forearc tectonics and volcanism during the Devonian–Carboniferous evolution of the North Patagonian segment, southern Chile (41,3°S)

C. Palape[1,2], P. Quezada[3], J. Bastías[4,5]*, F. Hervé[6,7], T. Reyes[6,8], M. Veas[6], F. Vildoso[9], M. Calderón[2], T. Theye[10], F. Fuentes[11] and M. Chiaradia[12]

[1]Departamento de Geología, Universidad de Oviedo, Oviedo, Spain, [2]Carrera de Geología, Universidad del Desarrollo, Las Condes, Chile, [3]Lamir Institute, Federal University of Paraná, Curitiba, Brazil, [4]Escuela de Geología, Facultad de Ingeniería, Universidad Santo Tomás, Santiago, Chile, [5]Department of Geology, School of Natural Sciences, Trinity College Dublin, Dublin, Ireland, [6]Departamento de Geología, Universidad de Chile, Santiago, Chile, [7]Carrera de Geología, Facultad de Ingeniería, Universidad Andrés Bello, Santiago, Chile, [8]Instituto de Geocronología y Geología Isotópica (CONICET-UBA) y FCFyN-Universidad de Buenos Aires, Buenos Aires, Argentina, [9]Departamento de Geofísica, Universidad de Chile, Santiago, Chile, [10]Institut für Anorganische Chemie, Universität Stuttgart, Stuttgart, Germany, [11]Consulting Geologist, Santiago, Chile, [12]Department of Earth Sciences, University of Geneva, Genève, Switzerland

Late Paleozoic to early Mesozoic subduction complexes formed during the evolution of southwestern Gondwana and extensively crop out along the Chilean continental margin. Recent findings in northern Patagonia (40°–43°S) revealed that accretionary processes were active since the Devonian when enhanced lithosphere stretching in the forearc led to the formation of Chaitenia island arc. The extension in the crust consecutively developed a backarc basin, which culminated during a compressive episode that re-amalgamated the Chaitenia island arc with the margin. This episode produced intermediate grade metamorphism in the sedimentary rocks that were formed throughout the extension. To constrain the tectonic evolution of these processes, we combined petrology, structural analysis, whole-rock geochemical, and whole-rock isotopic tracing (Sr-Nd-Pb) data along with thermodynamic modelling. Two petro-tectonic domains are here defined. The Western Coastal Range Domain is composed of Carboniferous to Permian metapsammopelitic rocks, which are mainly schists with a metasedimentary Carboniferous protolith exhibiting a penetrative northeast to southwest dipping main foliation associated with basal accretion. The Eastern Coastal Range Domain is comprised by garnet micaschists, metabasalts, metarhyolites, and metasandstones. This unit is folded by three ductile structures: The first is related to rootless isoclinal folds, the second is associated with kilometric scale west-verging tight folds, and the third is associated with west-verging cylindrical folds. The volcanic rocks of this domain are comprised by middle Devonian alkaline metarhyolites and metabasalts with enriched-MORB and

normal-MORB affinities. Trace element composition suggests that the metabasalts formed through shallow melting in an extensional setting over a supra-subduction zone. Nd and Pb isotope data point to a mantle source change for the basaltic melts from an EM1-like to a DM-like and are interpreted to reflect the embryonic to mature evolution of the early Devonian to Carboniferous backarc system. The calculated P–T evolution of the garnet micaschists follows: 1) a clockwise IP–IT prograde Barrovian path, 2) an isobaric thermal increase at ~7 kbar and 540°C, and 3) an adiabatic decompression. Finally, after the metamorphism, these rocks were uplifted by thrusting processes that probably occurred during the late Permian.

KEYWORDS

forearc basin, backarc basin, magmatism, metamorphism, structure, basin closure, accretionary orogen evolution, Chaitenia island arc

1 Introduction

Accretionary orogens are developed in convergent plate boundaries where an oceanic lithosphere is being subducted below a continental or an oceanic lithosphere, and their long-term evolution is marked by the tectonic-mode switching between advancing and retreating stages (e.g., Collins, 2002; Cawood et al., 2009; Ramos, 2009). These tectonics modes are dominated by the position evolution of the subducted plate with respect to the overriding plate. When the accretionary orogen is under an advancing and retreating mode, it may lead to compressional and extensional tectonics, respectively. Compressional deformation affects the upper plate, leading to crustal thickening and eventual inland arc magmatism migration (Gianni and Luján, 2021). Alternatively, extensional processes may lead to outward trench and arc migration with respect to the overriding plate (e.g., Schellart, 2008). Furthermore, enhanced extension and lithospheric thinning in the overriding plate may also lead to the development of marginal basins (Schellart et al., 2019), which are characterized by the formation of transitional crusts with supra-subduction and MORB-like geochemical affinities (Deng et al., 2017). While in most cases the locus of the initial rifting in the overriding plate occurs in the arc or the backarc (Molnar and Atwater, 1978; Taylor and Karner, 1983), rifting and oceanic lithosphere development in the forearc has also been proposed to occur during trench retreat, although less common (e.g., Taylor and Martinez, 2003). As the subduction system shifts to an advancing stage, it will develop compression that will focus in those areas that were thermally affected during the previous extension (i.e., the backarc; Dalziel, 1981). This compression may result in a re-amalgamation of the outwarded forearc, which will lead to a compressional climax (e.g., Brown, 2007). This process may also produce an intermediate pressure–temperature gradient metamorphism in the units located in the collision focus, which usually are those formed during the extension stage (e.g., Hyndman, 2019). This metamorphism is different from the typical high pressure–temperature (high P/T) and low pressure–temperature (low P/T) gradients found in the paired metamorphic subduction belts (Angí et al., 2010).

During the Devonian to the early Carboniferous, the margin of South America was part of the Terra Australis Orogen (Cawood et al., 2009), a large geological unit that still pose questions on the nature of the margin dynamics during this period. Particularly, it is a challenge to define the specific tectonic setting along the proto-Andes sector during this period. Furthermore, north of 27°S, a continental passive margin setting was proposed based on the absence of magmatic and metamorphic pulses (Bahlburg and Hervé, 1997; Creixell et al., 2021). However, recent findings of volcanic arc lavas on this sector of the margin with E-MORB and OIB metabasalts in the accretionary complexes have been interpreted to be formed in a retreating active margin (Fuentes et al., 2018; Bahlburg, 2021). Between 27° and 39°S, the Chilenia microplate, a hypothetical terrane with Laurentian affinity (Ramos et al., 1984), has been proposed to collide at ca. 390–374 Ma against the proto-margin of southwestern Gondwana (Ramos et al., 1986; Willner et al., 2011; Heredia et al., 2016). The suture of this collision has been proposed to be located to the east of the current Andes along a mafic-ultramafic belt (Boedo et al., 2021; Pérez Luján et al., 2021), which is complemented with the presence of the Guarguaráz complex eclogitic rocks (Figure 1A) that show the metamorphism associated with this collision (Massonne & Calderón, 2008; Willner et al., 2011). Alternatively, Dalhquist et al. (2021) revisited the age and geochemical magmatic evolution of this margin segment and suggested advancing and retreating subduction stages that were developed in an accretionary continental margin. The North Patagonian segment (39°–43°S) is limited to the north by the Lanalhue Fault (Figure 1A), where subduction was active during the Lower Devonian to early Carboniferous (Pankhurst et al., 2006; Hervé et al., 2016), and an abundant detrital zircon record of these ages is found in the late Paleozoic metamorphic complexes of this margin segment (Hervé et al.,

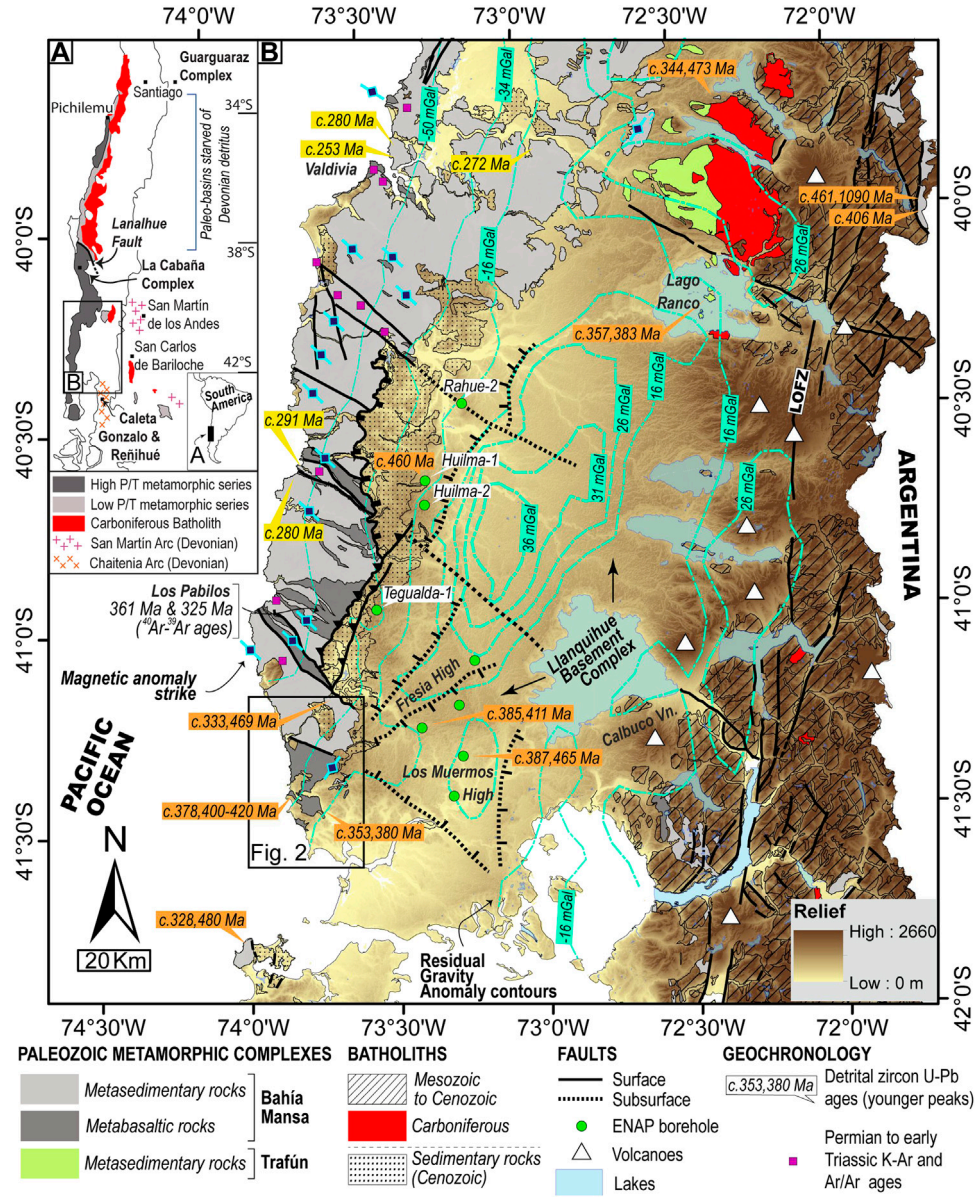

FIGURE 1
(A) Regional sketch map of south-central Chile showing the distribution of the Paleozoic igneous and metamorphic basement. The location of the Devonian arcs of San Martin and Chaitenia is highlighted. **(B)** Geological map of the Región de Los Lagos based on SERNAGEOMIN (2002). The subsurface fault traces and borehole locations are based on the work of Elgueta et al. (2000). LOFZ: Liquiñe-Ofqui Fault Zone. The residual gravity anomaly contours are based on the work of Yañez & Rivera (2019). The magnetic anomaly strike is based on the work of Godoy & Kato (1990). The detrital zircon U-Pb ages are from the work of Hervé et al. (2013; 2016; 2018) and Romero et al. (2020). K-Ar and Ar/Ar ages after Duhart et al. (2001) and the references therein.

2018). Recently, two Devonian plutonic belts with contrasting geochemical and isotopic tracing signatures have been identified to the west and east of the North Patagonian Andes. The eastern belt is slightly older and mostly composed of calk-alkaline granitoids associated with an active margin (San Martin arc; Rapela et al., 2021). The western belt is mostly composed of sub-alkaline tonalites that are associated with metabasaltic pillow lavas and metaturbidites (Hervé et al., 2018; Rapela et al., 2021). This led Rapela et al. (2021) to propose the opening of an oceanic

marginal basin in the forearc, which evolved to the formation of the Chaitenia island arc. Nevertheless, relevant questions remain regarding to the mechanisms and evolution throughout the oceanic basin development and later closure. To help to better understand these questions, we present here a combination of petrological, structural, geochemical, and isotopic tracing data along with thermodynamic modelling of relevant units that record the dynamics occurring in the margin during this process. Our results track the magmatic response to lithospheric thinning from initial continental extension to a mature backarc marginal basin. We interpret this to be associated with a retreating subduction setting, which eventually shifted to an advancing mode that resulted in the basin closure accompanied by a metamorphic event.

2 Geological setting

2.1 Regional background

Along the Chilean margin, between 34° and 43°S, paleo-subduction complexes crop out in the Coast Range (González-Bonorino, 1970; Hervé, 1988, Figure 1A). These are comprised of two units of contrasting nature, the Western and Eastern series (Aguirre et al., 1972), formed during the late Carboniferous to early Mesozoic (Hervé, 1988; Duhart et al., 2001; Willner et al., 2005; Hervé et al., 2013).

The Western Series (WS) is constituted by sedimentary, basaltic, and minor ultramafic rocks incorporated into the subduction channel and metamorphosed under high pressure–low temperature peak metamorphic conditions (HP–LT; 7–9.3 kbar and 380–420°C; Willner, 2005). The Eastern Series (ES) corresponds to continental-derived turbidites deposited in the trench and forearc settings, affected by the low-grade regional metamorphism (Hervé et al., 1984; Willner, 2005) with sporadic preservation of the primary sedimentary features of the protolith (González-Bonorino, 1970; Aguirre et al., 1972; Hervé, 1977). The metamorphic fabric of the WS is characterized by a S_2 main foliation with ubiquitous recrystallization and transposition of earlier primary and tectonic fabrics (Richter et al., 2007; Muñoz-Montecinos et al., 2020), while in the ES, the metamorphic fabric is characterized by tight upright folds related to subvertical S_1 foliation/cleavage and occasionally development of less steep S_2 foliation (Hervé et al., 1988; Richter et al., 2007). The difference in the deformation style and strain among the two series is interpreted to be related to distinct modes of accretion in the subduction wedge; the WS is formed by a basal accretion mechanism at deeper levels in the crust, and the ES is formed by frontal accretion at shallower crustal depths (Richter et al., 2007). The ES is intruded by the calc-alkaline granitoids of the late Carboniferous Coastal Batholith (e.g., Deckart et al., 2014) that generates the low pressure–high temperature (LP–HT: 2–4 kbar and 300–550°C; Hyppolito et al., 2015) metamorphic overprint on the previous regional metamorphism (Hervé, 1977; Martin et al., 1999; Willner, 2005; Hyppolito et al., 2015).

South of Lanalhue Fault (Figure 1A), the Western and Eastern series are represented by the Bahía Mansa Metamorphic Complex (BMMC; Duhart, 1999) and by the Trafún Metamorphic Complex (Campos et al., 1998; Martin et al., 1999; see Figure 1B), respectively. Late Paleozoic forearc accretion is recorded in the BMMC due to the presence of Upper Mississippian to Permian detrital zircon maximum depositional ages in the sedimentary protolith of the BMMC (Hervé et al., 2013; Hervé et al., 2016; Hervé et al., 2018; Romero et al., 2020). At the Los Pabilos locality (41°S, Figure 1B), exotic boulders of coarse-grained blueschists with relict eclogite-amphibolite mineral assemblages are found in unconsolidated sediments deposited over a serpentinite body interleaved with mafic schists (Kato and Godoy, 1995). An amphibole $^{40}Ar/^{39}Ar$ plateau age of 361 ± 1.7 Ma (late Devonian) obtained in a retrograde garnet-bearing amphibolite facies mineral assemblage within the exotic blueschist was interpreted as the minimum age for the onset of subduction at these latitudes, while the blueschists facies overprint would have occurred at ca. 320–325 Ma (Kato et al., 2008). Willner et al. (2009) determined an anticlockwise PT-path in an exotic garnet amphibolite boulder in the same area, calculating peak metamorphic conditions at 12–14 kbar and 600–700°C. Furthermore, they dated HP–LT metamorphism at ca. 340 Ma Lu/Hf (garnet) with isobaric cooling at ca. 305 Ma (Rb/Sr mineral isochron). Permian to Triassic K-Ar, Rb-Sr, and Ar/Ar ages (Figure 1) in the BMMC are interpreted to be associated with the regionally distributed greenschists facies retrograde metamorphism that followed the HP–LT phase (Duhart et al., 2001). The regional trend of the aeromagnetic anomaly in the BMMC has a NW-SE strike (Figure 1B), and it is associated with the S_2 fabric of the metamorphic complex with similar structural tendency; tectonic slices of serpentinites and mafic schists are composed of highly magnetic zones (Godoy and Kato, 1990).

The oldest rocks out cropping in the Chilean portion of the North Patagonian segment (39°–43°S) are the Chaitenia arc-backarc system (Hervé et al., 2016; 2018; Rapela et al., 2021). The Chaitenia island arc magmatism expands between ca. 395 and 355 Ma (Rapela et al., 2021), and the age of inception of backarc oceanic floor spreading is constrained in the Reñihue Fjord area (Figure 1A) and is dated between ca. 395 and 390 Ma by U-Pb SHRIMP detrital zircon ages of metasedimentary rocks intercalated with the basaltic pillow-lavas (Hervé et al., 2018; Rapela et al., 2021), which is in accordance with the nearby occurrence of slate boulders containing Lower Devonian trilobites (Fortey et al., 1992). The Early Devonian igneous rocks in the Chaitenia arc-backarc system corresponds to Caleta Gonzalo diorite, located near Reñihue and was formed at 392 ± 3 Ma (Rapela et al., 2021; Figure 1A) and the Zarao

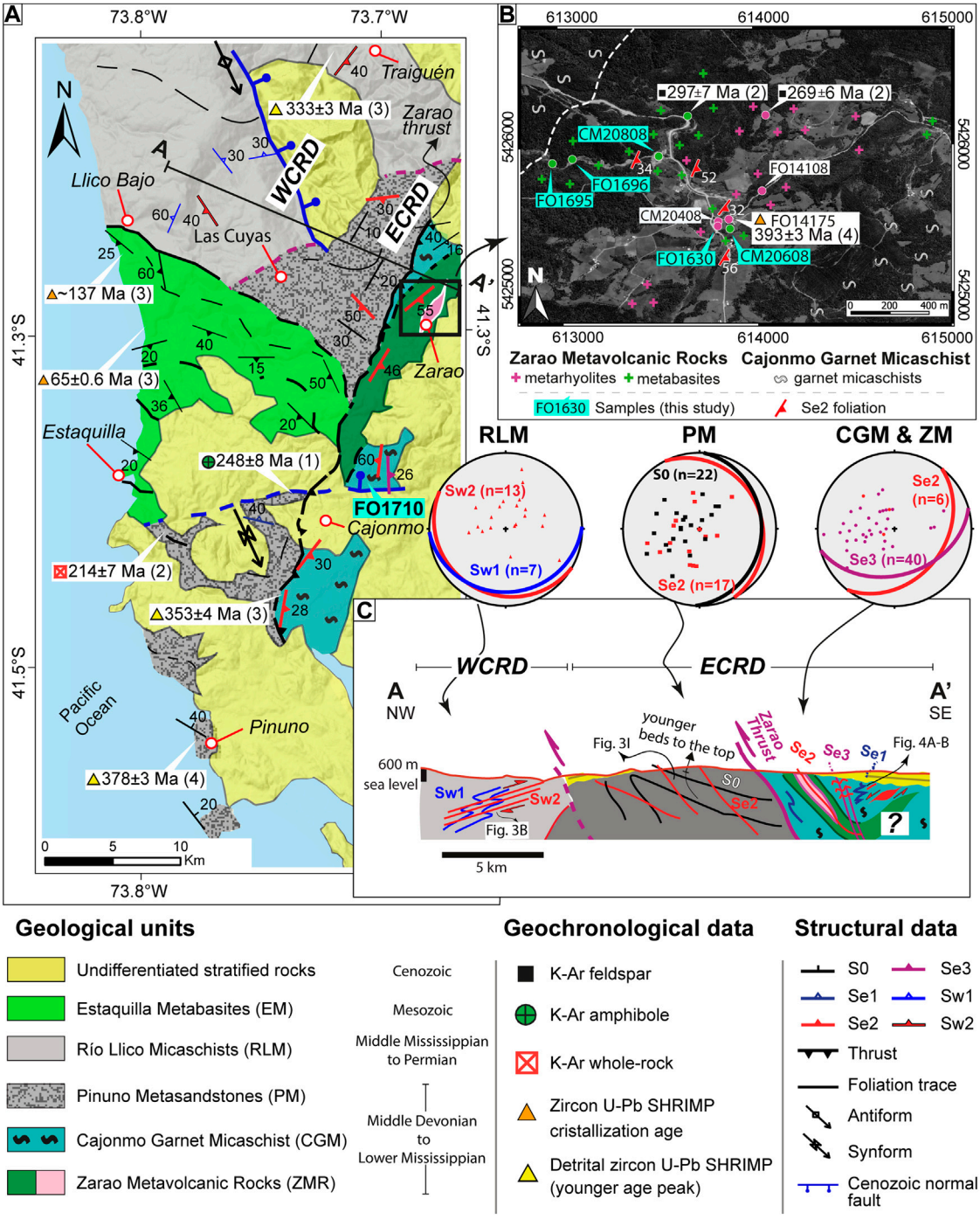

FIGURE 2
(A) Geological map of the area generated in this study. Geochronological data after 1) Duhart et al. (1997), 2) Duhart et al. (2001), 3) Hervé et al. (2016), and 4) Hervé et al. (2018). The location of the sample used for thermodynamic modelling is shown. **(B)** Zoom-in view of the Zarao area. The sample location used for geochemical and isotopic tracing studies is shared along with the location of metarhyolite samples reported by Rapela et al. (2021). **(C)** Simplified cross section of the studied area, and its location is shown in **(A)**. Structural data are projected in lower hemisphere equal-angle stereonets.

metarhyolite (393 ± 3 Ma, Hervé et al., 2018; Figure 2A). Furthermore, at the La Cabaña complex (Figure 1A), polydeformed mafic and ultramafic rocks (Plissart et al., 2021) with backarc basin geochemical signatures (Höfer et al., 2001; González-Jiménez et al., 2014) are intercalated with metasedimentary schists with abundant Devonian detrital zircons (Romero et al., 2020) and may correspond to the northernmost known exposures of the Chaitenia arc/backarc system. The late Mississippian (ca. 330–323 Ma) continental arc located at similar latitudes to the east of the main Andes (Pankhurst et al., 2006) is interpreted as a time-marker for the minimum age of closure of the Chaitenia backarc basin (Rapela et al., 2021).

2.2 Geology of the study area

The study area is located in the southern portions of the Coast Range (Figure 2), where metamorphic units previously assigned to the Bahía Mansa metamorphic complex crop out (BMMC, Duhart, 1999). The surface geological data are complemented with metamorphic rock samples recovered from well cores drilled few to tens of km east of the range (Figure 1B). The area is separated in two domains based on geochronological, lithological, metamorphic, and structural features: the Western Coastal Range Domain and the Eastern Coastal Range Domain (details are given below). These domains are in contact by the west border of the Pinuno Metasandstones, which has been interpreted as a reverse fault.

2.2.1 Western Coastal Range Domain

The Western Coastal Range Domain comprises the metamorphic rocks that crop out mostly in the western flank of the Coast Range (Figure 2). Two units with different lithological and structural characteristics have been defined by Duhart (1999). The Estaquilla Metabasites correspond to nematoblastic mafic schists with N-MORB geochemical signature (Crignola et al., 1997) and Cretaceous to early Cenozoic U-Pb zircon crystallization ages (Hervé et al., 2016) metamorphosed at greenschist facies. The Río Llico Micaschists are composed of fine interlayers of metasandstones and metapelites with greenschist facies mineral associations of quartz-white mica-albite and quartz-albite-chlorite interleaved with minor NW-SE trending nematoblastic to granonematoblastic greenschist bodies with an actinolite-epidote-chlorite-quartz-albite assemblage (Duhart, 1999). Hervé et al. (2016) obtained a ca. 330 Ma zircon U-Pb maximum depositional age based on a micaschist of this unit (Figure 2A).

2.2.2 Eastern Coastal Range Domain

The Eastern Coastal Range Domain is composed of the Zarao Metavolcanic Rocks (Vildoso, 2017) and the neighboring garnet-bearing micaschist (Palape, 2020), which we define as the Cajonmo Garnet Micaschist. The metavolcanic rock unit is constituted by the Zarao metarhyolite and the spatially associated mafic schists (Figure 2). The crystallization age of the igneous protolith of the Zarao metarhyolite is constrained by 396.7 ± 1.3 Ma U-Pb age (Duhart et al., 2001) and 393 ± 3 Ma U-Pb SHRIMP age (Hervé et al., 2018) and corresponds to the oldest unit in the area. The metarhyolite has been interpreted to be either formed in an ocean island environment (Quezada et al., 2018) or a continental forearc rift setting (Rapela et al., 2021). In the Zarao area (Figure 1B), the aeromagnetic anomaly has a NE-SW strike, which differs with the NW-SE regional pattern of magnetic anomalies (Godoy and Kato, 1990).

Located at the east of the Coast Range, buried under the Cenozoic sedimentary cover, the Llanquihue Basement Complex (Duhart et al., 2001) was recognized in the exploration boreholes (Elgueta et al., 2000). It is mostly composed of micaschists with Devonian detrital zircon U-Pb maximum depositional age (Quezada, 2015; Hervé et al., 2016; 2018). Duhart et al. (2001) report the existence of an undeformed hornblende tonalite with ca. 359 Ma (Ar/Ar in hornblende) crosscutting micaschists at the bottom of the Rahue-2 borehole (Figure 1B). Geophysical surveys show the existence of an NNE-SSW-trending dense block at depths (Tašárová, 2007; Yañez and Rivera, 2019; Maksymowicz et al., 2022), which is interpreted as the subsurface extension of the Llanquihue Basement Complex (Figure 1B). The northern limit of this basement complex is located near Lago Ranco where the Trafún Metamorphic Complex crops out (Figure 1B), and the latter shares a significative Devonian component in the detrital zircon age population (Hervé et al., 2016). The Trafún Metamorphic Complex is intruded by the late Carboniferous coastal batolith, where Deckart et al. (2014) reported a U-Pb SHRIMP age of 306 ± 1 Ma.

3 Methods

The geological recognition of the metamorphic rocks in the area was based on the map of Duhart et al. (1999), which was improved with the new data of this study (Figure 2A). Six rock samples of the Llanquihue Basement Complex (Figure 1B) were recovered from hydrocarbon exploration boreholes provided by ENAP (Empresa Nacional del Petróleo) for petrographic analysis. Three of the well cores have been previously dated by Hervé et al. (2016) and Hervé et al. (2018), yielding Devonian maximum depositional ages. The abbreviation for names of rock-forming minerals created by Whitney & Evans (2010) was used.

10.3389/feart.2022.873785

TABLE 1 Bulk rock geochemical analysis of the Zarao Metavolcanic Rocks.

	Alk rhyolite	P-MORB	P-MORB	E-MORB	N-MORB
Major oxides (wt%)					
SiO_2	62.1	54.9	50.9	46.3	51.2
Al_2O_3	15.2	18.8	14.4	14.6	16.5
Fe_2O_3(T)	3.72	7.75	10.9	10.5	7.66
MnO	0.16	0.14	0.14	0.16	0.16
MgO	0.12	3.89	5.65	10.7	6.2
CaO	1.03	9.51	11.7	8.58	11.4
Na_2O	4.99	4.21	2.48	2.09	3.55
K_2O	5.51	0.95	0.76	0.63	0.34
TiO_2	0.36	1.42	1.72	0.99	0.7
P_2O_5	0.06	0.21	0.24	0.1	0.06
Cr_2O_3	0	0.01	0.02	0.06	0.06
NiO	0	0.01	0.01	0.03	0.01
LOI	5.89	1.83	2.71	4.8	1.85
Total	99.0	104	102	99.5	99.7
Trace elements (ppm)					
Co	0.57	26.6	35.4	51.2	27.2
Rb	60.0	22.2	17.3	19.2	11.6
Sr	177	251	511	280	206
Y	201	24.8	27.3	17.6	17.1
Zr	1,322	124	146	50.0	32.8
Nb	103	14.9	17.9	4.73	0.50
Cs	0.77	0.90	0.69	0.83	0.20
Ba	436	255	181	259	109
La	181	17.6	19.5	5.72	1.33
Ce	334	35.3	40.6	11.2	4.11
Pr	33.9	4.21	4.92	1.57	0.74
Nd	126	18.5	21.3	7.43	4.32
Sm	21.6	4.33	4.89	2.07	1.54
Eu	1.81	1.36	1.53	0.82	0.82
Gd	21.1	4.78	5.34	2.64	2.22
Tb	3.38	0.71	0.84	0.47	0.41
Dy	25.2	4.73	5.24	3.21	2.89
Ho	5.81	0.91	1.03	0.68	0.63
Er	18.7	2.51	2.88	1.97	1.84
Tm	2.86	0.36	0.41	0.3	0.28
Yb	19.4	2.35	2.72	2.04	1.84
Lu	2.98	0.34	0.4	0.29	0.27
Hf	25.1	3.06	3.78	1.31	0.96
Ta	5.56	0.89	1.12	0.29	0.04
Th	23.9	2.54	2.93	0.45	0.03
La/Sm_N	5.29	2.56	2.5	1.74	0.54
Sm/Yb_N	1.19	1.97	1.92	1.09	0.89
Eu/Eu*	0.26	0.91	0.92	1.07	1.36
Ce/Y	1.66	1.43	1.48	0.64	0.24
Isotope geochemistry					
$^{87}Sr/^{86}Sr_t$	0.7061	0.7065	0.7068	0.7068	0.7055
εNd_t	−3.04	−2.89	−1.65	3.29	7.63

(Continued on following page)

TABLE 1 (*Continued*) Bulk rock geochemical analysis of the Zarao Metavolcanic Rocks.

	Alk rhyolite	P-MORB	P-MORB	E-MORB	N-MORB
$^{206}Pb/^{204}Pb_t$	18.11	17.9	17.8	17.99	17.8
$^{207}Pb/^{204}Pb_t$	15.63	15.6	15.61	15.64	15.57
$^{208}Pb/^{204}Pb_t$	38.97	38.74	38.69	38.01	37.15

TABLE 2 Major (wt%) element composition of the garnet bearing micaschist FO1710 sample used for pseudosection calculations.

wt% initial	
SiO_2	62.27
Al_2O_3	18.86
MnO	0.06
MgO	1.63
CaO	0.93
Na_2O	2.08
K_2O	4.11
TiO_2	0.75
P_2O_5	0.13
Fe_2O_3	5.85
CO_2	-
H_2O	-
Sum	94.79

3.1 Structural analysis (mesoscale and microscale)

The metamorphic basement in the study area exhibits superposed ductile structures. To identify these structures, the geometrical relationships as bedding vs. foliation or foliation vs. foliation were used (Bell, 1981; McClay, 1987). This was complemented with the kinematic criteria obtained from the asymmetric shear sense indicators to determine the vergence of the structure of ductile deformation. We have used the structures of ductile deformation for morphology rather than deformation phases, as emphasized by Tobisch and Paterson (1988), not to dismiss progressive deformation phases that can individually develop into two or more ductile structures. Mesoscale structural fieldwork data were complemented with the microstructural-petrographic analysis of thin sections, where a numerical index was used to depict the stages of structure development (see the work of Fossen et al., 2019) combined with letter subscripts referring to the structural domain. For example, Sw1 and Se2 denotes foliation S1 of the Western Coastal Range Domain and foliation S2 of the Eastern Coastal Range Domain, respectively. The aim of this nomenclature is to separate the structures that occur in units of different ages. To understand the relation and relative timing between the deformation and metamorphic mineral formation, the criteria proposed by Passchier and Trouw (2005) were used.

3.2 Bulk rock geochemistry

Five representative rock samples of the Zarao Metavolcanic Rock unit were collected (Figure 2B), and the analytical data are compiled in Table 1. Rock powders were prepared using an agate mill, and major and trace elements were measured using a Philips PW2400 X-Ray Fluorescence (XRF) spectrometer at the University of Lausanne, Switzerland. The NIMN, NIMG, BHVO, and SY2 standards were used for quality control. Glass-fused disks prepared for XRF analyses were fragmented and mounted for additional analyses of trace and rare earth elements (REEs) by LA-ICP-MS. Measurements were made using an Agilent 7,700x quadrupole ICP-MS, and depending on the expected concentration within samples, either NIST SRM 610 or 612 reference material glasses were used as external standards. The laser settings employed in these analyses employed a 10 Hz repetition rate and a spot size of between 80 and 120 µm. Blanks were measured for ~90 s, after which the laser was switched on and the signal was measured for 45 s. The Sr or Al_2O_3 concentrations (as previously determined by XRF) were used as an internal standard. Each sample was ablated three times, and average concentrations were calculated offline using LAMTRACE (Jackson, 2008). The uncertainties of three spots per sample are ±10% for rare earth elements (REEs) and ±5% for other trace elements. Whole rock compositions have been normalized to an anhydrous state in all diagrams. The new data are integrated with the whole-rock geochemistry of pillow metabasalts and mafic schists presented by Rapela et al. (2021).

Sample FO1710 (garnet micaschist) was analyzed for the P–T pseudosection modelling with a Philips PW2400 XRF spectrometer at the University of Stuttgart (Germany) using a glass disc prepared with bulk rock powder. The composition results are presented in Table 2.

TABLE 3 Representative analyses of the garnet, plagioclase, and ilmenite from the FO1710 garnet bearing mica schist sample.

Mineral	Garnet # 1			Garnet # 2			Plagioclase		Ilmenite		
Location/Type	Core	Middle	Rim	Upper rim	Core	Bottom rim	In matrix	In matrix	In Se2	In Se2	In Se2
SiO_2	36.77	36.98	37.15	37.09	37.47	37.26	62.92	66.23			
TiO_2	0.07	0.01	0.01	0.03	0.02	0.00	0.00	0.04	53.31	52.66	52.66
Al_2O_3	20.99	21.10	21.23	21.09	21.22	21.14	23.86	20.50	0.00	0.00	0.00
Cr_2O_3	0.04	0.04	0.01	0.01	0.03	0.00	0.00	0.00	0.01	0.00	0.00
FeO	30.27	30.50	32.34	31.57	32.30	32.22			44.53	42.47	42.47
Fe_2O_3	0.22	0.00	0.00	0.00	0.00	0.00	0.06	0.28	0.00	0.00	0.00
MnO	8.63	8.14	6.59	6.44	6.41	6.33			2.06	2.30	2.30
Mn_2O_3							0.00	0.01			
MgO	1.54	1.59	1.66	1.49	1.71	1.61	0.00	0.00	0.05	0.02	0.02
CaO	2.30	2.02	1.84	2.14	1.88	1.86	5.01	1.17			
Na_2O	0.01	0.05	0.02	0.04	0.02	0.02	8.91	11.11			
K_2O							0.05	0.06			
BaO							0.04	0.00			
V_2O_3									0.00	0.00	0.00
NiO									0.00	0.00	0.00
Total	100.84	100.42	100.85	99.89	101.07	100.45	100.85	99.40	99.96	97.45	97.45
Si	58.99	59.73	59.78	60.50	60.36	60.44	27.63	29.25			
Ti	0.01	0.00	0.00	0.00	0.00	0.00	0.00	0.00	10.13	10.27	10.27
Al	39.69	40.17	40.27	40.54	40.28	40.41	12.35	10.67	0.00	0.00	0.00
Cr	0.00	0.01	0.00	0.00	0.00	0.00	0.00	0.00	0.00	0.00	0.00
Fe^{3+}	0.03	0.00	0.00	0.00	0.00	0.00	0.00	0.01	0.00	0.00	0.00
Fe^{2+}	40.61	41.19	43.52	43.06	43.51	43.71			0.94	0.92	0.92
Mg	0.37	0.38	0.40	0.36	0.41	0.39			0.00	0.00	0.00
Ca	0.40	0.35	0.32	0.37	0.33	0.32	0.24	0.06			
Mn	11.72	11.13	0.90	0.89	0.87	0.87			0.04	0.05	0.05
Na	0.00	0.02	0.01	0.01	0.01	0.01	0.76	0.95			
Mn^{3+}							0.00	0.00			
Ba							0.00	0.00			
K							0.00	0.00			
V									0.00	0.00	0.00
Ni									0.00	0.00	0.00
X (Grs)	0.07	0.06	0.05	0.06	0.05	0.05					
X (Prp)	0.06	0.06	0.07	0.06	0.07	0.07					
X (Alm)	0.68	0.69	0.73	0.72	0.73	0.73					
X (Sps)	0.20	0.19	0.15	0.15	0.15	0.15					
X (An)							0.24	0.06			
X (Alb)							0.76	0.94			
X (Kfs)							0.00	0.00			

Garnet normalized to 24 O and 16 cations. Plagioclase normalized to 8 O. Ilmenite normalized to 3 O.

3.3 Sr–Nd–Pb bulk rock isotopes

100 mg of whole rock powder was dissolved in 4 ml of concentrated HF and 1 ml of 15 M HNO_3 in closed Teflon vials at 140°C for 7 days. The samples were dried down and re-dissolved in 3 ml of 15 M HNO_3 before being dried down again. Sr–Nd–Pb chemical separation followed the methods described in the work of Pin and Santos-Zalduegui (1997) and Chiaradia et al. (2011). Isotopes of Sr, Nd, and Pb were analyzed at the University of Geneva using a Thermo Neptune PLUS Multi-Collector ICP-MS following the methods described by Béguelin et al. (2015) and Chiaradia (2015). Isotopic ratios

TABLE 4 Representative analyses of white mica, biotite, chlorite, and epidote from the FO1710 garnet bearing mica schist sample.

Mineral	White mica			Biotite		Chlorite		Epidote
Location/ Type	In Se2 foliation	In Se2 foliation	In Se1 foliation	In Se2 foliation	Post-Se2 foliation	In Se2 foliation	In Se2 foliation	In Se1 foliation
SiO_2	47.78	46.85	46.57	34.09	32.95	23.94	26.11	35.67
TiO_2	0.28	0.33	0.21	1.62	1.40	0.08	0.07	0.72
Al_2O_3	32.93	34.54	35.91	17.96	17.72	22.92	20.28	25.61
Cr_2O_3	0.00	0.00	0.00	0.00	0.00	0.00	0.00	0.00
FeO	2.05	1.76	1.47	24.69	25.04	29.45	29.42	
Fe_2O_3								12.84
MnO	0.00	0.00	0.02	0.09	0.12	0.24	0.16	0.00
Mn_2O_3	0.00	0.00	0.00	0.00	0.00	0.00	0.00	0.09
MgO	1.31	0.97	0.71	7.50	8.23	11.86	11.05	0.01
CaO	0.00	0.00	0.00	0.00	0.03			21.61
Na_2O	0.64	0.74	1.09	0.04	0.08			0.01
K_2O	10.51	10.59	10.22	8.76	7.40			
BaO	0.28	0.31	0.34	0.16	0.09			
H_2O	4.51	4.52	4.55	3.81	3.75	11.23	11.09	1.86
Total	100.29	100.61	101.09	98.72	96.80	99.71	98.18	
Si	3.18	3.11	3.07	1.34	1.32	2.56	2.83	2.87
Alt	0.82	0.89	0.93	0.66	0.68	1.44	1.17	0.01
Alo	1.76	1.81	1.86	0.02	0.02	1.44	1.41	2.29
Ti	0.00	0.00	0.00	0.00	0.00	0.00	0.00	0.00
Fe^{2+}	0.01	0.01	0.01	0.81	0.84	2.63	2.66	
Fe^{3+}				0.00	0.00			0.08
Mn	0.00	0.00	0.00	0.00	0.00	0.00	0.00	
Mn^{3+}				0.00	0.00			0.00
Mg	0.01	0.01	0.01	0.04	0.05	1.89	1.78	0.00
Ca	0.00	0.00	0.00	0.00	0.00			1.86
Ba	0.00	0.00	0.00	0.00	0.00			
Na	0.01	0.01	0.01	0.00	0.00			0.00
K	0.89	0.90	0.86	0.04	0.04			
X (Ms)	0.69	0.74	0.74					
X (Wm-Phl)	0.02	0.02	0.02					
X (Cel)	0.10	0.06	0.04					
X (FeCel)	0.09	0.06	0.04					
X (Pg)	0.08	0.10	0.14					
X (TiMnCaWm)	0.02	0.02	0.02					
X (Ps)								0.24
#Fe				0.65	0.63	0.58	0.60	

White mica normalized to 22 O, and assuming Fetotal = Fe2+. Biotite normalized to 22 O, and assuming Fetotal = Fe2+. Chlorite normalized to 28 O, and assuming Fetotal = Fe2+. Detection limit up to 0.1 wt%.

were corrected for internal fractionation using $^{88}Sr/^{86}Sr$=8.375,209 for the $^{87}Sr/^{86}Sr$ ratio, $^{146}Nd/^{144}Nd$=0.7219 for the $^{143}Nd/^{144}Nd$ ratio, and $^{203}Tl/^{205}Tl$=0.418,922 for the three Pb ratios (a Tl standard was added to the solution). SRM987 ($^{87}Sr/^{86}Sr$=0.710248, long-term external reproducibility: 10 ppm), JNdi-1 ($^{143}Nd/^{144}Nd$= 0.512115; Tanaka et al., 2000; long-term external reproducibility: 10 ppm), and SRM 981 (Pb-isotopes; Baker et al., 2004; long-term external reproducibility of 0.0048% for $^{206}Pb/^{204}Pb$, 0.0049% for $^{207}Pb/^{204}Pb$, and 0.0062% for $^{208}Pb/^{204}Pb$) were used as external standards. Due to a

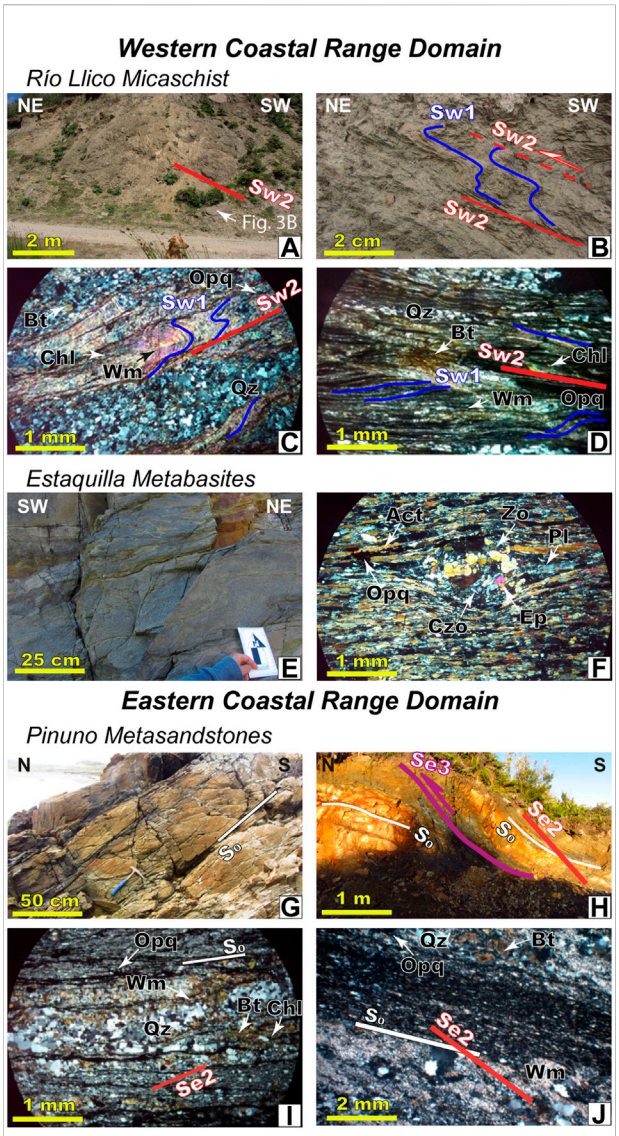

FIGURE 3
(A) Roadcut of the Río Llico Micaschists, where the main foliation Sw2 dips 40° to the W. **(B)** Zoom-in view of **(A)** that shows the foliation Sw1 crenulated by the Sw2 main foliation where the shear sense is top-up-to-the-northeast. **(C,D)** are thin sections of the Río Llico Micaschists, where the cleavage domain is formed by white mica, biotite, and chlorite, which crenulated the previous Sw1 foliation **(C)**, and Sw1 is oblique to Sw2 **(D)**. **(E)** Llico Bajo coastal outcrop of the Estaquilla Metabasites with folded bands of different mineral sizes. **(F)** Porphyroblasts of plagioclase with asymmetric strain shadows of chlorite surrounded by actinolite in a nematoblastic texture. **(G)** Representative coastal outcrop of the Pinuno Metasandstone unit in the Pinuno locality showing the alternating layers of coarse grain metasandstones (thick brownish beds) with medium to fine grain heterolithic sandstones (thin gray beds), and the bedding S0 dips 60° to the NE. **(H)** Small quarry of the Pinuno Metasandstones where the foliation Se2 dips more than the bedding S0 with 40° SE dipping, cut by a fault assigned to the Se3 foliation. **(I,J)** are thin sections collected of the outcrops presented in **(A,B)**, respectively, showing a minor obliquity between the Se2 cleavage domain and S0 plane.

systematic difference between measured and accepted standard ratios, Sr, Nd, and Pb isotope ratios were further corrected for external fractionation by values of −0.039, +0.047, and +0.5 amu, respectively. Mass interferences at 84 (^{84}Kr), 86 (^{86}Kr), and 87 (^{87}Rb) were corrected by monitoring ^{83}Kr and ^{85}Rb. The interference of ^{144}Sm on ^{144}Nd was monitored on ^{147}Sm and corrected with a value of 0.206,700 (^{144}Sm/^{147}Sm). The interference of ^{204}Hg on ^{204}Pb was corrected by monitoring ^{202}Hg. The data are expressed as time corrected initial isotope ratios based on the c. 393 Ma U-Pb zircon SHRIMP crystallization age obtained by Hervé et al. (2018) for the Zarao metarhyolite, which is considered as the age of the protolith of the Zarao Metavolcanic Rocks.

3.4 Electron probe micro-analyzer

The major element compositions of garnet, white-mica, biotite, and chlorite of a garnet micaschist of the Cajonmo Garnet Micaschist (sample FO1710) were measured using a CAMECA SX100 electron microprobe (EMP) with five wavelength-dispersive spectrometers at Universität Stuttgart, Germany. Operating conditions were set at a 15 kV acceleration voltage with a beam size of 1–5 µm. A beam current of 15 nA was used for garnet and 10 nA for other silicate minerals. The elements analyzed were Si, Ca, Al, Na, K, Mg, Mn, Fe, Ti, and Cr. The standards used to calibrate these analyses were: wollastonite (Si, Ca), synthetic Al_2O_3 (Al), albite (Na), orthoclase (K), synthetic MgO (Mg), natural hematite (Fe), rhodonite (Mn), synthetic TiO_2 (Ti), and synthetic Cr_2O_3 (Cr).

The major element concentration maps in garnet were acquired by the stepwise movement of the sample under a stationary electron beam of the microprobe and subsequent computer-assisted evaluation with the XMAP program of Bernhardt et al. (1995). For the calculation of cationic proportion of the oxides, the computer program CALCMIN (Brandelik, 2009) was applied. Representative mineral compositions are presented in Tables 3, 4.

4 Results

4.1 Field relationships, lithology, and petrography

4.1.1 Western Coastal Range Domain

4.1.1.1 Río Llico Micaschist

The Río Llico Micaschists crop out in the northern edge of the study area (Figure 2A). Although it was not possible to visit

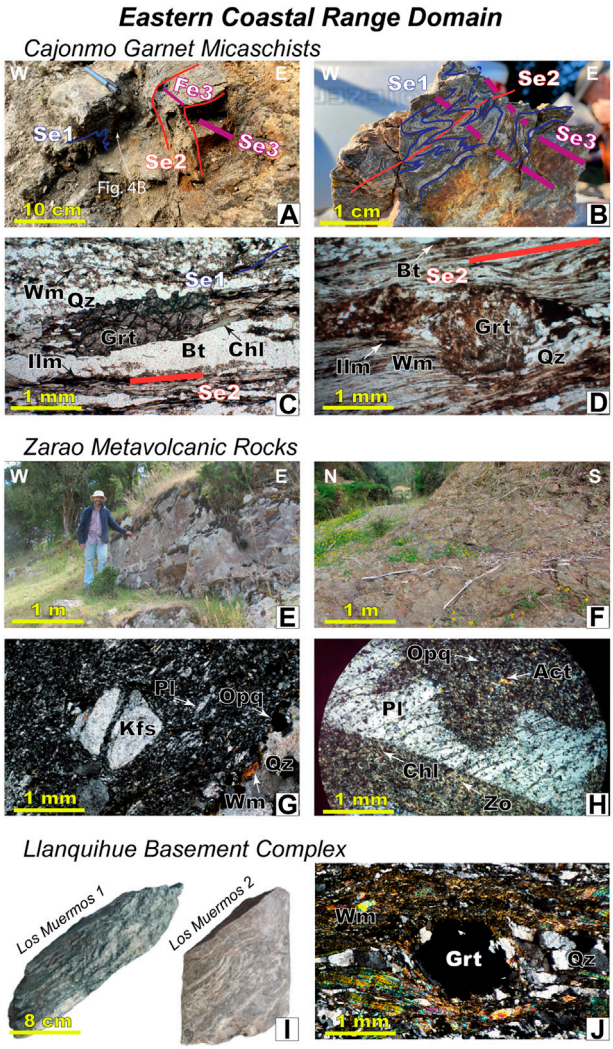

FIGURE 4
(A) Roadcut outcrop of Cajonmo Garnet Micaschist, where the main Se3 foliation dips 40° to the east. **(B)** Zoom-in view of **(A)** showing the parasitic S-type folds associated with the Fe2 isoclinal, where the foliation Se1 dips 60° to the west and the foliation Se2 dips 40° to the west. **(C)** Thin section of **(A)**, which shows a minor angularity between the Se1 and Se2 foliation with post-tectonic garnet porphyroblasts. **(D)** Thin section of Pinuno Metasandstones in the Zarao range, which shows a porphyroblast of garnet with asymmetric strain shadows of quartz surrounded by chlorite, white mica, and biotite in a lepidogranoblastic texture. **(E)** Isolated body of metarhyolite in the Zarao Metavolcanic Rocks. **(F)** Metabasites of the Zarao Metavolcanic Rocks, in a creek of the Zarao range. **(G)** Thin section of outcrop presented in **(E)**, revealing a porphyritic texture constituted by potassic feldspar phenocrystals with microlites of plagioclase in a glassy groundmass. **(H)** Thin section of the outcrop presented in **(F)** showing metamorphic and igneous texture, as oriented actinolite with zoisite in a fine nematoblastic and reabsorption textures observed in an inherit plagioclase phenocrystal, respectively. **(I)** Samples of psammopelitic schists in ENAP's boreholes located in the Los Muermos and Fresia High along the eastern side of the Coast Range. **(J)** Thin section of sample HU1-T8 presented in **(I)** that exhibits a syn-tectonic porphyroblast of garnet with asymmetric strain shadows of quartz surrounded by chlorite, white mica, and biotite in a lepidogranoblastic texture.

the contact of this unit with Pinuno Metasandstones, it is inferred as a reverse fault. This unit corresponds to psammopelitic schists with well-defined 1–3 mm-thick mineral banding with no preservation of the sedimentary structures of the protolith at mesoscale (Figures 3A,B). The metamorphic mineral assemblage is composed of Qz+Wm+Bt+Chl+Pl+Ep+Ap+Ttn+Opq (Figure 3C) in a lepidogranoblastic texture. The microstructure of the rocks is characterized by quartz bands and microlithons alternating with mica-rich layers (Sw2). The Sw1 structures are preserved as crenulations between the micaceous Sw2 cleavage domains (Figure 3D).

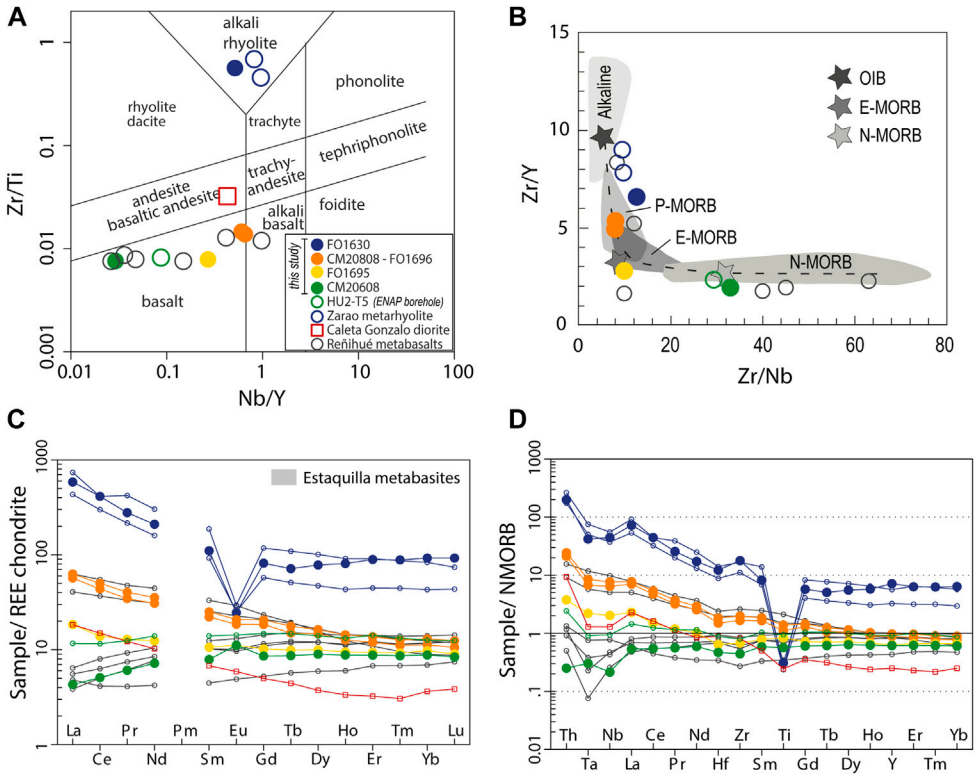

FIGURE 5
Solid circles correspond to the samples analyzed in this study. The open symbols correspond to the data obtained from the literature: Zarao metarhyolite, Caleta Gonzalo diorite, and Reñihue metabasalts (see Figure 1A for the location) are from the work of Rapela et al. (2021), and HU2-T5 metabasalt (see Figure 1B for borehole location) is from the work of Quezada (2015). **(A)** Zr/Ti vs. Nb/Y classification diagram (Winchester and Floyd, 1977; modified by Pearce, 1996). **(B)** Zr/Y vs. Zr/Nb diagram for metabasalts and metarhyolites analyzed. The composition of N-MORB, E-MORB, and OIB is from the work of Sun and McDonough (1989). Composition of fields for N-MORB, E-MORB, P-MORB, and alkaline (ocean-island basalts) and the dashed line representing the mixing curve between the OIB and N-MORB end members is from Saccani et al. (2014) and references therein. **(C)** REE spider diagram normalized to chondrite (Boynton, 1984). The gray field of the Estaquilla Metabasites is after Crignola et al. (1997). **(D)** Multi-element spider diagram normalized to the N-MORB composition of Sun and McDonough (1989), following the criteria proposed by Pearce (2014).

4.1.1.2 Estaquilla Metabasites

This unit is in the central part of the study area (Figure 2A), and the main exposures are found along the shoreline and coastal cliffs. To the north the limit is marked by a reverse fault that sits the Estaquilla Metabasites on top of the Río Llico Micaschists, while to the south, its contact with the Pinuno Metasandstones is covered and it is interpreted to be related to Cenozoic E-W normal faulting. The most common lithology corresponds to green-colored nematoblastic metabasites with a well-developed foliation marked by aligned actinolites (Figure 3E). The basaltic protolith was metamorphosed under greenschist facies with the formation of the Act+Chl+Zo+Pl+Ttn+Ep+Opq+Qz mineralogical assemblage (Figure 3F). At microscale, actinolite–chlorite grains define an anastomosing and asymmetrical foliation. Some plagioclase crystals showing myrmekite texture are interpreted as relict features of the protolith. Because the uncertainty of the Estaquilla Metabasite age, it is not considered in this work.

4.1.2 Eastern Coastal Range Domain

4.1.2.1 Pinuno Metasandstones

This unit is composed by alternating layers of coarse to medium grain metasandstones with medium to fine grain heterolithic sandstones in decimeter thick beds. Metapelite layers of 5–30 cm-thick interdigitated with metasandstones have also been recognized (Figure 3G). The preservation of the sedimentary structures of the protolith is a common feature in the unit. Normal grading is ubiquitous in the metasandstones and indicates a normal upright position. The metapelite rip-up clasts were recognized in the metasandstones, while planar lamination and cross-lamination were observed in the heterolithic sandstones. At mesoscale, the cleavage of the rocks is poorly developed and intersects intersects the bedding (S0) at low angle. The metasandstones are composed by Qz+Wm+Bt+Chl+Pl+Ep+Opq, and at microscale, the cleavage is marked by fine grained aligned crystals of biotite

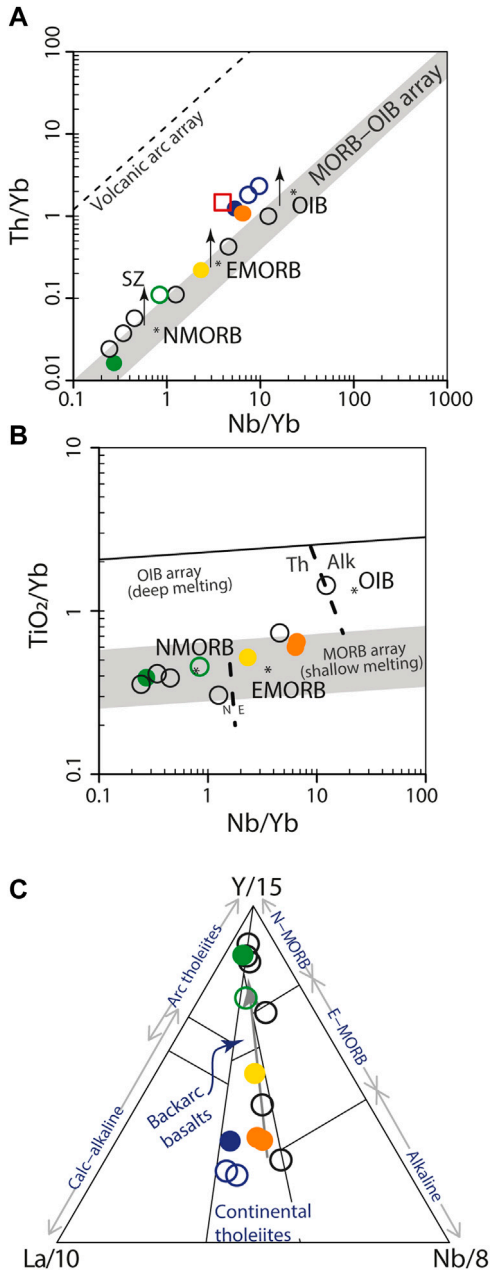

FIGURE 6
(A,B) Th/Nb vs. Nb/Yb and TiO_2/Yb vs. Nb/Yb diagrams of Pearce (2008). The composition of the Zarao metarhyolites is plotted for its comparison. SZ: subduction zone influence. The OIB, E-MORB, and N-MORB composition of Sun and McDonough (1989) is shown for comparison. **(C)** Y–La–Nb tectonic discrimination diagram of Cabanis and Lecolle (1989). The composition of the Zarao metarhyolite is shown for comparison. The gray arrow shows the expected evolutionary trend for the magmatism from a continental setting to a backarc setting. Same symbols as in Figure 5.

and white micas (Figure 3I). The chlorites and biotites grew at the expense of white micas as mimetic growth in the main Se2 foliation.

4.1.2.2 Cajonmo Garnet Micaschist

The Cajonmo Garnet Micaschist is an NNE-trending semicontinuous belt mostly composed by pelitic and psammopelitic schists is recognized along road cuts and E-W fault creeks (Figure 2A). The schists exhibit two penetrative foliations (Figures 4A,B) and are composed by Qz+Bt+Wm+Chl+Grt+Pl+Ilm+Ep+Ap+Opq arranged in a lepidogranoblastic texture defining the Se2 foliation (Figure 4C). At microscale, some garnet porphyroblasts show sigma pressure shadows and sigmoidal pseudomorphs fully replaced by micaceous minerals (Figure 4D), which are oblique to the previous foliation (Se1) and overprinted by the Se2 main foliation. The main Se2 foliation is characterized by spaced schistosity with a zonal cleavage domain composed mainly of white mica with quartz and scarce plagioclase microlithons separated by quartz bands. The white micas and quartz bands show sigmoidal shape developed in the Se2 main foliation. The garnet porphyblast rims are in contact with Wm+Ilm+Qz+Bt+Pl and shows no strain shadows (Figures 8A,B). The shape of garnet porphyroblasts is rectangular elongated along the schistosity, and their boundaries are mostly straight but in contact with the quartz bands have few embayed borders (Figures 8A,B). Most garnet, biotite, and chlorite porphyroblasts are recrystallized over of the main Se2 foliation, showing no deflection between the internal and external Se2 foliation. The chlorites and biotites grew at the expense of white mica as mimetic growth along oriented phyllosilicates and crystallized oblique to the main Se2 foliation.

4.1.2.3 Zarao Metavolcanic Rocks

The Zarao Metavolcanic Rocks are composed of mafic schists, metabasites, and minor metarhyolites cropping out in an NNE-SSW oriented belt of c. 22 km^2 (Figure 2A). The Cajonmo Garnet Micaschists were recognized surrounding the exposures of metavolcanics rocks, but the contact between both units has not been identified in the field (Figure 2). This contact is interpreted as the western flank of a synform and is further discussed later in the text.

The metarhyolites crop out as isolated bodies of few tens-to-hundreds of meters between the mafic schists and metabasites (Figure 2B), and their field relationships are not observed. At outcrop scale, the rocks most commonly show poorly developed foliation planes (Figure 4E) and feldspar phenocrysts (up to 1 cm) immersed in a gray-to-pink colored silicified microcrystalline groundmass. Locally, the metarhyolite is brecciated evidencing late-stage deformation under the brittle regime. At microscale, the fragmented K-feldspar crystals show Carlsbad twinning and perthitic texture and the groundmass is composed of subhedral feldspar microliths together with

Fsp+Qz+Opq+Chl+Wm+Bt (Figure 4G). In addition, plagioclase and minor quartz phenocrysts are preserved, highlighting the quartz-saturated composition of the igneous protolith. Few yellowish subhedral garnet porphyroblasts (<0.3 mm) occur in veins containing green-colored biotite. Scarce prismatic pseudomorphs replaced by biotite, epidote, and garnet, and opaque minerals may be relics of magmatic pyroxene or amphibole crystals.

At mesoscale, the metabasaltic rocks are green colored with orange oxidation surfaces due to weathering (Figure 4F). Some exhibit nematoblastic textures with the development of penetrative foliation planes, while others have granoblastic textures and massive fabrics at outcrop scale: The first are more common in the eastern sector, while the latter are more common in the west. Actinolite schists as well as tremolite schists compose the unit. Relics of the igneous protolith are preserved in the granoblastic metabasites. They correspond to 0.25–0.5 mm plagioclase crystals, some of them with reabsorption textures, partly replaced by <0.1 mm epidote and clinozoisite/zoisite grains, and 3–5 mm K-felspar crystals with Carlsbad twinning and albite intergrowths (perthites), and the latter replaced by <0.01 mm zoisite/clinozoisite and clay minerals (Figure 4H). Furthermore, <0.3 mm pseudomorphs fully replaced by zoisite/clinozoisite have pseudo-hexagonal shapes and are probably relicts of igneous Ca-rich pyroxenes. Poorly developed cleavage planes observed in the metabasites suggest two foliations affecting the unit.

4.1.2.4 Llanquihue Basement Complex

The lithology of the Llanquihue Basement Complex is addressed through three samples located in the Los Muermos and Fresia high areas (Figure 1B), few km east of the study area, and other three samples are located to the north, along the eastern slope of the Coast Range (Figure 1B). They correspond to lepidoblastic psammopelitic schists and one nematoblastic metabasite recovered from the Huilma 2 borehole (sample HU2-T5 in Figures 5, 6). The schists have a well-developed main foliation Se1 overprinted by Se2 crenulation composed of the micas, folds, and microfolds mostly oblique to Se1, but subparallel in one borehole at Los Muermos High (Figure 4I). The mineral assemblage consists in Qz+Wm+Ab+Ttn+Ep+Tur+Zrn for the schist at Los Muermos/Fresia highs (Figure 4J), Act+Czo+Sme+Opq in the metabasite sample (HU2-T5), and Qz+Wm+Grt+Chl/Sme+Tur+Ap+Zrn in the micaschist samples near the Coast Range (Huilma-1 and Tegualda-1 boreholes, Figure 1B). The occurrence of sigmoidal white mica and syn-kinematic garnets developed the Se2 foliation in the Huilma-1 borehole suggest similarities with the Se2 foliation observed in the Cajonmo Garnet Micaschists.

4.2 Structure of the metamorphic basement

4.2.1 Western Coastal Range Domain

The metamorphic fabric of the Río Llico Micaschists is constituted by two foliations, Sw1 and Sw2. In the western sector of this unit (Figure 2), the foliation Sw1 dips 70°NW and is crenulated by foliation Sw2 that dips 40°W (Figures 3A,B). The L2 lineation formed by the intersection of the Sw1 and Sw2 foliations dips 42° to the SW. Parasitic Z type microfolds related to the Sw2 axial plane crenulation (Figure 3C) are facing to the SW. The sigmoidal shape of the microfolds indicates top-up-to-the-northeast (i.e., reverse-sense) shear (Figure 3B), as shown by Bell and Johnson (1992) for determination of the shear sense of crenulation development in a fold limb. The mineral stretching lineation associated with the Sw2 dips 20° to the SW. In addition, the Sw1 foliation at microscale is anastomosed and oblique to the Sw2 foliation (Figure 3D).

In the eastern sector of this unit (Figure 2), the Sw1 foliation dips 40° to SE, while the Sw2 foliation dips 20°E. The structure associated with the Sw2 foliation of this unit is part of a kilometric scale northeast-vergent duplex thrust sheets. The contact between the Río Llico Micaschists and Pinuno Metasandstones is inferred to be related to a later west-vergent thrust (Figure 2C).

4.2.2 Eastern Coastal Range Domain

Three foliations (Se1, Se2, and Se3) are recognized in the Cajonmo Garnet Micaschist unit, while only the Se2 structures are present in the Zarao Metavolcanic Rock unit. The Se1 structures in the Cajonmo Garnet Micaschist are rootless isoclinal folds of centimetric and millimetric wavelength (Figures 4A,B, 8B). The Se2 foliation is formed by an asymmetric foliation that dips 60° to the W (Figures 4A,B) and folds the previous Se1 foliation in parasitic isoclinal S-type folds that face to the W. At microscale, the foliation Se2 is anastomosed and envelopes a few syn tectonic garnet porphyroblasts with asymmetric sigma tails (Figure 4D); however, most garnet crystals have post-tectonic textural features (Figure 4C). In addition, the sigmoidal shape of the Se2 micas and quartz bands indicate top-down-to-the-west shear sense representing a reversed normal limb of a west-vergent Fe2 isoclinal fold (Figures 2C–4B–4B). The Se2 foliation is folded by cylindrical Fe3 tight folds. A displacement between the pelitic and psammopelitic layers was recognized in their hinge, produced by the flexural slip. These cylindrical folds develop a 40°E dipping Se3 axial plane crenulation cleavage representing an inverse limb of a west-vergent fold (Figures 2C–4B–4B). The contact between the Cajonmo Garnet Micaschists and Zarao Metavolcanic Rocks lies in the west flank of the Fe3 synform. While this contact may be tectonic or interlayed, further fieldwork is required to define it. The fold axes Fe3 are conformed by the intersection of the Se2 and Se3 foliation planes and dip 15° to the south

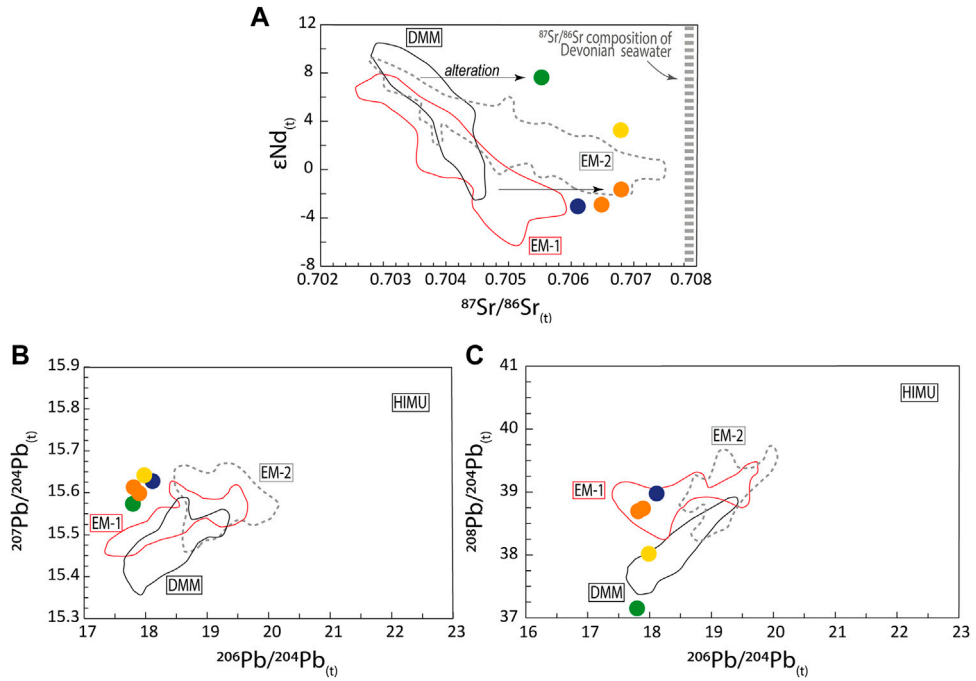

FIGURE 7
Time corrected (*t*= 393 Ma) whole-rock isotope composition of the Zarao Metavolcanic Rocks. The compositional fields for DMM (Depleted MORB Mantle), EM-1 (Enriched Mantle 1), and EM-2 (Enriched Mantle 2) correspond to compiled analysis from modern oceanic island basalts erupted at the "type localities" for each mantle "reservoir" (modified from the work of Hofmann, 2014). The $^{87}Sr/^{86}Sr$ composition of Devonian seawater is from the work of McArthur et al. (2012).

(Figure 4A). A detailed analysis of the (micro)structure and metamorphic mineral growth is given in Section 4.4. The deformation of the Se3 foliation is coherent with the ductile thrusting responsible of sitting the Cajonmo Garnet Micaschist together with the Zarao Metavolcanic Rocks above the poorly deformed Pinuno Metasandstones (Figure 2C).

The structures of the Pinuno Metasandstones are well exposed at the Las Cuyas locality (Figure 2A). They are poorly deformed and exhibit a 30° SE-dipping Se2 cleavage. The preserved sedimentary structures indicate a normal position of the beds, and bedding (S0) dips 50° to the SE (Figures 3G,H). The angular relationship between the Se2 cleavage and the bedding S0 is observed at microscale as well (Figures 3I,J). Hence, the exposed outcrops of the Pinuno Metasandstones represent the normal limb of the NW-vergent kilometric structure (Figure 2C).

4.3 Geochemistry of the Zarao Metavolcanic Rocks

All the data are summarized in Table 1. The analyzed samples have variable LOI wt% values between 1.83 and 5.89%, and the higher content is displayed by the Zarao metarhyolite (sample FO1630). To avoid the effects of post-magmatic alteration that can strongly modify the original geochemical signature of the protolith, the presented data will mostly be focused on low mobility elements (e.g., Pearce, 2014 and the references therein).

4.3.1 Major and trace element

The SiO_2 content of the metarhyolite is ~66 wt% and in the metabasaltic rocks ranges between ~49 and 54 wt%; among the latter, the higher contents (~52–54 wt%) correspond to samples FO1696 and CM20608. The metabasalts have FeO_t (FeOt = 0.9 * Fe_2O_{3T}) values between 6.9 and 10.08 wt%, MgO between 3.85 and 11.41 wt%, CaO between 9.17 and 11.99 wt%, and K_2O+ Na_2O values between 2.91 and 5.11 wt%. In terms of major element composition, sample FO1695 is the less fractionated and samples FO1696–CM20608 are the most evolved.

The metarhyolite is enriched in Zr (1,322 ppm) and has a Nb/Y ratio of 0.51, and its protolith is classified as an alkaline rhyolite (Figure 5A; Winchester and Floyd, 1977; modified by Pearce, 1996). The chondrite-normalized REE pattern (Figure 5C) shows a steep pattern for the LREE (La_N/Sm_N= 5.29), a nearly flat pattern for the HREE (Sm_N/Yb_N= 1.19), and a pronounced Eu negative anomaly (Eu/Eu*= 0.26). The N-MORB-normalized

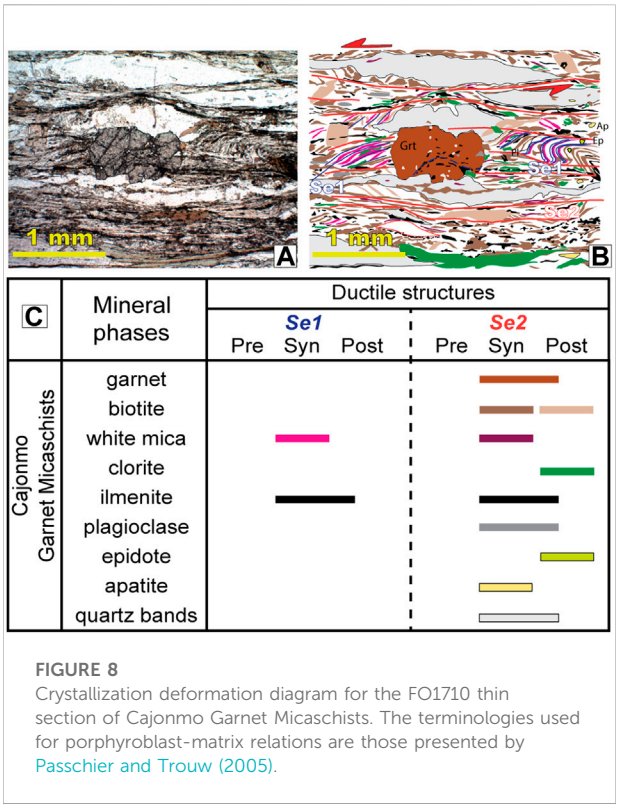

FIGURE 8
Crystallization deformation diagram for the FO1710 thin section of Cajonmo Garnet Micaschists. The terminologies used for porphyroblast-matrix relations are those presented by Passchier and Trouw (2005).

multi-element pattern (Figure 5D) is characterized by a negative Nb-Ta anomaly, a small Zr positive anomaly, and a marked Ti negative anomaly.

Based on the Ti/Zr and Nb/Y ratios, the protoliths of the metamafic rocks correspond to subalkaline basalts (Figure 5A; Winchester and Floyd, 1977; modified by Pearce, 1996). Samples FO1696 and CM20808 have Nb/Y values of 0.6–0.65 and yield compositions close to the alkali basalt field. The Zr/Y and Zr/Nb ratios (Figure 5B) point to three types of basaltic protoliths like, normal mid-ocean ridge basalts (N-MORBs), enriched mid-ocean ridge basalts (E-MORBs), and plume-type MORB (P-MORB), the latter transitional between E-MORB and alkaline oceanic within plate basalts (OIBs). The chondrite-normalized REE pattern shows significant differences among the metabasaltic rocks. The metabasalts with E-MORB and P-MORB like signatures are enriched in LREE (La_N/Sm_N= 1.74 and ~2.5, respectively), while the N-MORB like is depleted in LREE (La_N/Sm_N= 0.54). On the other hand, the HREE pattern of N-MORB and E-MORB like is nearly flat (Sm_N/Yb_N= 0.89 and 1.09, respectively) when compared to the more step pattern in the P-MORB like metabasalts (Sm_N/Yb_N ~ 1.95). A marked Eu positive anomaly is displayed by the N-MORB like (Eu/Eu*=1.36) and a subtle one by the E-MORB (Eu/Eu*=1.07). Furthermore, the P-MORB-like metabasalt has a small negative Eu anomaly (Eu/Eu* ~0.91). The N-MORB like shows a Nb negative anomaly, while the others display coupled Nb-Ta negative anomalies. The P-MORB like basalt has a small negative anomaly of Ti, and the E-MORB and N-MORB like basalts have small negative anomalies of Hf-Zr (Figure 5D).

4.3.2 Sr-Nd-Pb isotopes

The $^{87}Sr/^{86}Sr_t$ isotope composition shows values between 0.7055 and 0.7067 (Figure 7A). These high values suggest that post-magmatic processes (hydrothermal/metamorphic events) have modified the original signature of the igneous protolith, particularly in the metabasaltic rocks, perhaps involving the participation of sea water. The εNd_t values have a wider range; the lowermost values correspond to the metarhyolite and the P-MORB (-3.04 to -1.64), while the metabasalts with signatures like E-MORB and N-MORB have positive values of 3.28 and 7.6, respectively (Figure 7A). The $^{207}Pb/^{204}Pb_t$ isotope composition has a narrow range of values between 15.57 and 15.64, as well as the $^{206}Pb/^{204}Pb_t$ composition with values between 17.79 and 18.11 (Figure 7B). A wider range of values is shown by the $^{208}Pb/^{204}Pb_t$; the metarhyolite and P-MORB have values between 38.69 and 38.97, while the E-MORB and N-MORB have values of 38.01 and 37.15, respectively (Figure 7C).

4.4 Microstructure and metamorphism of the Cajonmo Garnet Micaschist

To establish the microstructure relationships and the P–T metamorphism conditions, we studied a garnet-bearing micaschist of the Cajonmo Garnet Micaschist (sample FO1710) (Figure 2A). The P–T conditions of the metamorphism were derived based on thermodynamic modeling of mineral equilibria. We considered the observed mineral parageneses, the composition of individual minerals, and the occurrence of reaction structures and textures between them.

4.4.1 Crystallization–deformation relationships and mineral chemistry

The sample FO1710 contains the mineral assemblage biotite + white mica + garnet + quartz + plagioclase + ilmenite ± epidote ± apatite ± chlorite (mostly retrograde). Garnet is up to 1 mm in diameter. The crystallization–deformation relationships and mineral paragenesis, shown in Figure 8, suggest the existence of two metamorphic episodes affecting the Cajonmo Garnet Micaschists. The essential metamorphic minerals formed in the De1 deformation event are white mica + ilmenite, constituting the folded foliation Se1. The metamorphic minerals formed in the Se2 comprise biotite + white mica + ilmenite aligned in the crenulation cleavage Se2 domain spaced by quartz and plagioclase microlithons (Figure 8B). According to the petrographic observations in Section 4.1.2.2, most garnets, chlorites, and epidotes are post-tectonic to the Se2 foliation. The Syn-Se2 garnet porphyroblasts exhibit an

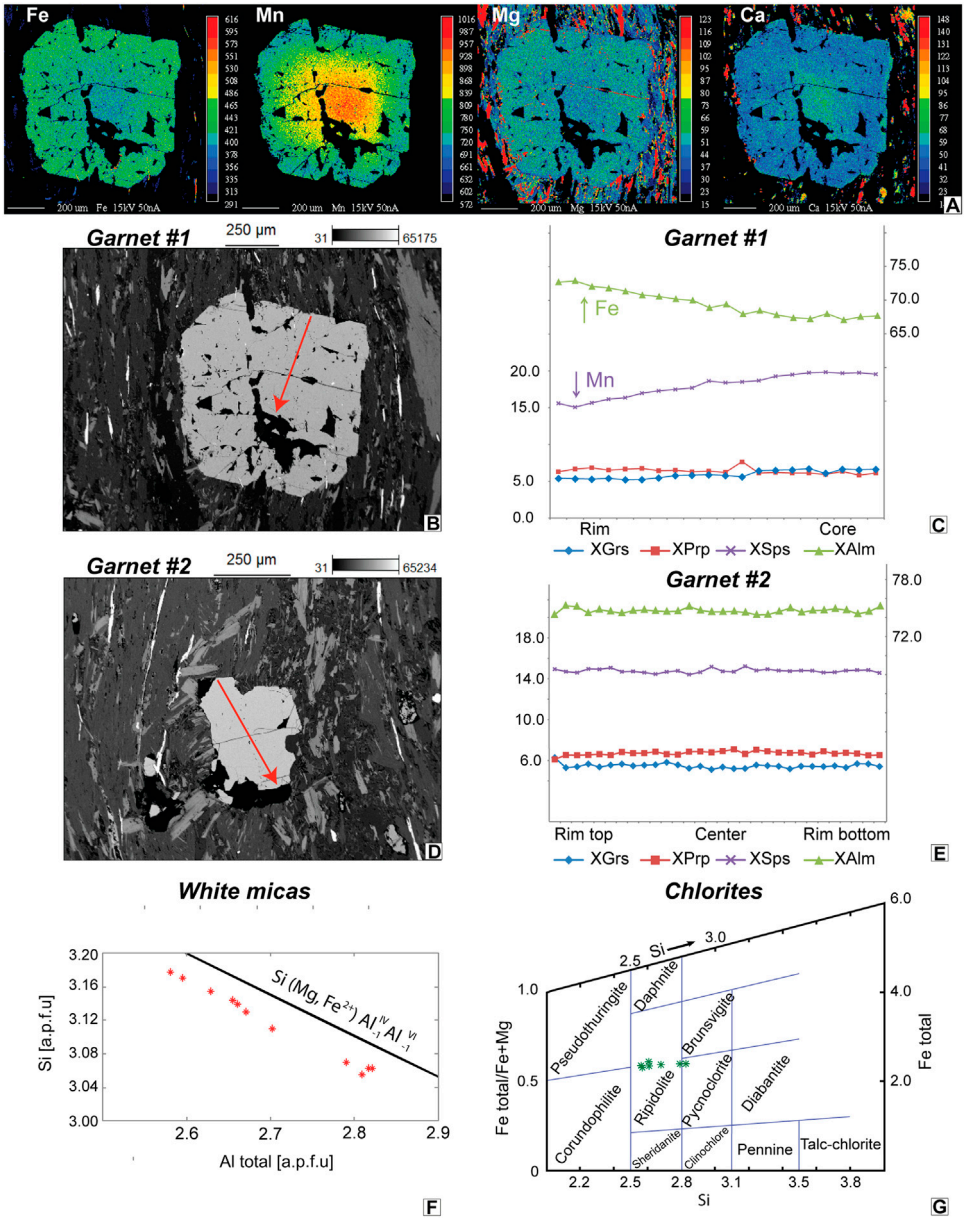

FIGURE 9
(A) Garnet element distribution maps of Fe, Mn, Mg, Ca concentration, obtained with CAMECA SX100. Colour scale refers to counts per second of corresponding Kα radiation, where the lowest and the highest concentrations are in blue and red, in that order. **(B)** SEM image with the analysed line beyond the garnet #1 porphyroblasts. **(C)** Chemical profile of the orange arrow of the Panel **(B)**. **(D)** SEM image with the analysed line beyond the garnet #2 porphyroblasts. **(E)** Chemical profile of the orange arrowof the Panel **(D)**. **(F)** Si–Al variation diagram of white-mica within garnet bearing micaschist (FO1710), the line of the ideal Tschermak substitution is inserted. **(G)** Si vs. XFe Chlorite classification diagram of Hey (1954), the green asterisk corresponds to chlorite of the FO1710 sample.

internal foliation (S1) formed by the inclusion of epidote, quartz, apatite, biotite, white mica, and ilmenite.

The chemical composition of garnet was analyzed along two profiles (Figures 9A–C). The Syn-Se2 garnet #1 is relatively large (500 µm). It is idiomorphic and shows straight borders, and the Se2 foliation is defined by biotite, white mica, and ilmenite wrapping around. Garnet #2 is smaller and post-tectonic. In the central part, garnet #2 contains a linear trail of inclusions, while close to the edge's inclusions are randomly oriented. The chemical analyses indicate that garnet is essentially almandine. Garnet #1, unlike garnet #2, exhibits a noticeable chemical zonation. Mn decreases from core to rim (X_{Sps} = 0.14–0.20),

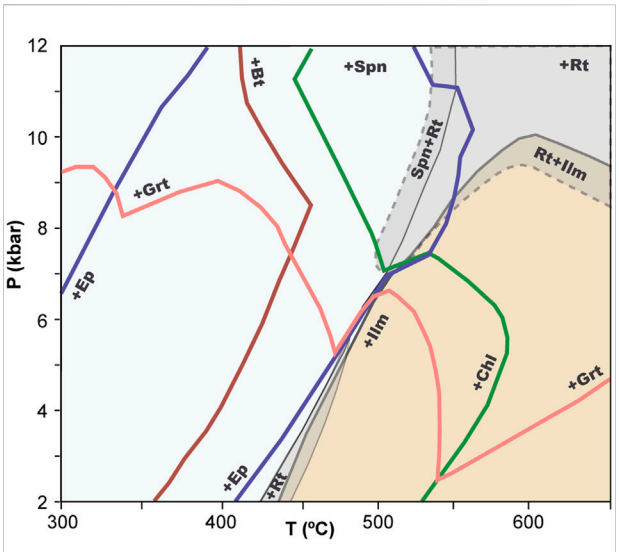

FIGURE 10
Major aspects of the calculated P–T pseudosection with PERPLE_X for the sample FO1710. The mineral abbreviation used was extracted from the work of Whitney and Evans (2010).

whereas Fe shows the opposite behavior (X_{Alm} = 0.67–0.73). Ca and Mg remain almost constant from the core to rim (X_{Grs} = 0.05–0.07; X_{Prp} = 0.06–0.08). Garnet #2 shows no chemical zonation; noteworthy, its composition essentially conforms to the rim of garnet #1. It should be noted that at the very edges of garnet #2, there is a decrease in X_{Alm} from 0.733 to 0.724 and X_{Prp} from 0.065 to 0.061, and an increase in X_{Sps} from 0.146 to 0.150 and X_{Grs} from 0.053 to 0.063 (Figure 9E).

The white mica and biotite analyzed are mainly in the foliation Se2 and occur as fine-grained crystals with lepidoblastic texture in mica-rich bands. On the basis of 11 oxygens for the structural formula, the white mica composition is essentially muscovite that is characterized by a considerable composition range: Si_{iv} = 3.06–3.18 per formula unit (pfu), Al_{iv} = 0.82–0.94, and Al_{vi} = 1.76–1.88 pfu. The compositional variation is mainly due to the Tschermak exchange (Si_{iv} + $(Mg, Fe^{2+})_{vi}$ = Al_{iv} + Al_{vi}) (Figure 9F). A slight deviation can be explained by the presence of minor amounts of ferric iron. Biotite occurs as fine-grained crystals in mica-rich bands. The biotite composition shows only little variation: Si_{iv} = 2.63–2.69 per formula unit (pfu) unit based on 11 oxygens, Al_{iv} = 1,30–1.36, Al_{vi} = 0.30–0.37 pfu, Ti_{vi} = 0.08–0.10 pfu, and X_{Fe} = Fe/(Fe+Mg) = 0.63–0.65. Plagioclase is scarce and occurs preferentially as microlithons in the granoblastic texture displaying an oligoclase to albite composition of X_{An} = 0.06–0.24. Ilmenite contains about 5% of the pyrophanite component. Retrograde chlorite replacing biotite shows composition with X_{Fe} = 0.57–0.60 (Figure 9G). The epidote is scarce and scatters on the granoblastic and lepidoblastic bands with a pistacite composition of X_{Ps} = Fe/(Fe+Al) = 0.24.

4.4.2 Pseudosection modelling and P–T constraints

For P–T evaluation, P–T and T–O_2 pseudosections were calculated using the thermodynamic Gibbs energy minimizing software Perple_X (downloaded 23.02.2022; Connolly, 1990; 2005) in the chemical system Mn-Na-Ti-Ca-K-Fe-Mg-Al-SiO-H-O, for a range from 2 to 12 kbar and 300 to 650°C. The thermodynamic database used was TC-DS633 by Holland & Powell (1998). The following solution models as provided by the Perple_X were applied: Gt(W) for garnet, Bi(W) for biotite, Chl(W) for chlorite, Mica(W) for white mica, Ilm(DS6) for ilmenite, feldspar, and Ep(HP11) for epidote.

For the calculation, the analyzed composition of the studied rock FO1710 from the Cajonmo Garnet Micaschists has been slightly corrected to fit the 11-component system. Furthermore, the CaO content was reduced according to the bulk-rock phosphorus content, assuming that these elements are bound to apatite (Calderón et al., 2017). Accordingly, the CaO content is reduced from 0.93 to 0.77 wt% (Table 2). To estimate the portions of FeO and Fe_2O_3, a T-O_2 pseudosection at 5 kbar was calculated (not shown). Owing to the presence of ilmenite and the absence of both hematite and magnetite, the portion of ferric iron is limited to values clearly lower than 10% of the total iron, in the temperature range under present consideration. A further constraint is given by the composition of epidote. Accordingly, for the calculation of P–T pseudosections, the amount of Fe^{3+} is set to 3% of total Fe (0.16 wt% Fe_2O_3). The water content is set sufficiently high to ensure the water-excess condition in the considered P–T span.

Figure 10 shows major aspects of the calculated P–T pseudosection for sample FO1710. The P–T conditions of the formation of garnet can be derived from the intersection of the X_{Sps} and X_{Prp} isopleth of this mineral (Figures 11A,B–H). The X_{Prp} isopleth indicates a temperature of 540°C, independent of pressure. A pressure of about 7 kbar is then derived from the intersection with the X_{Sps} isopleth. This P–T condition is valid for the core and rim of the large garnet as well as for the small garnet, which all have the same Ca and Mg contents. The increase of Mn from the core to rim in garnet #1 may therefore reflect a Rayleigh fractionation of Mn during growth of garnet at constant P–T of 7 kbar/540°C (Figure 11A). Iron then behaves complementary to Mn. Noteworthy, the derived P–T of garnet growth is close to the low-T stability limit of the garnet. The onset of garnet growth there corroborates the interpretation of fractionation, causing the zonation of this mineral, supported by the X_{Sps} = 0.20 garnet core isopleth that does not intersect with Mg and Ca garnet core isopleths, showing non-equilibrium conditions. In addition, the derived P–T is compatible with the presence of biotite, plagioclase with oligoclase composition (Figure 11D), chlorite (Figure 11F), epidote (Figure 11G), and ilmenite. Because the

10.3389/feart.2022.873785

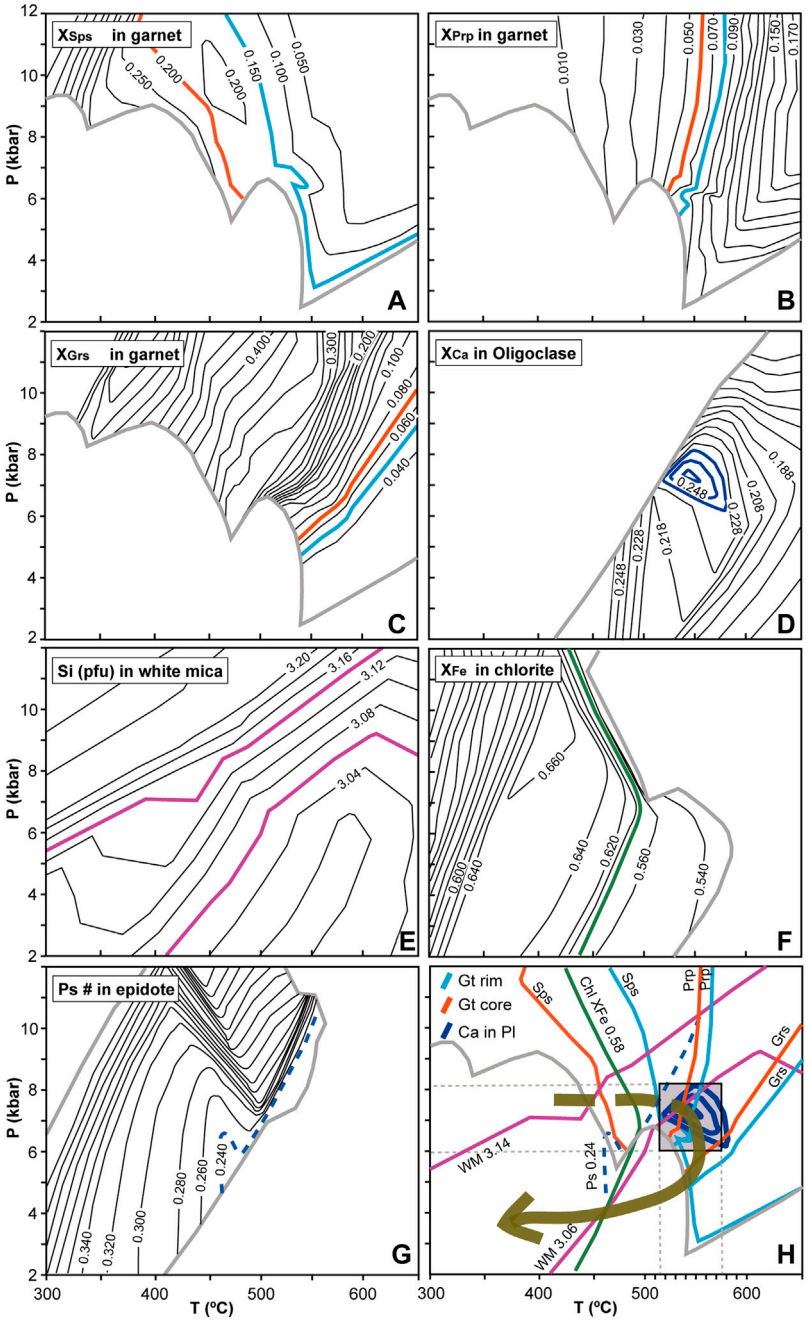

FIGURE 11
Calculated isopleths of mineral composition for the sample FO1710 with PERPLE_X. Selected isopleths for the thermodynamic model are presented in X_{Sps} in the garnet **(A)**, X_{Prp} in the garnet **(B)**, and X_{Grs} in the garnet **(C)**, which show the model of core and rim garnet composition in orange and light blue, respectively. The garnet stability field limit is presented in gray. Following diagrams show the selected isopleths of X_{Ca} in oligoclase **(D)**, Si (pfu) in white mica **(E)**, X_{Fe} in chlorite **(F)**, and Ps # in epidote **(G)**, which are presented in blue, purple, green, and dashed blue lines, respectively. The mineral stability limits are presented in gray. **(H)** Thermodynamic model obtained by the information gathered in **(A–F)** showing relevant isopleths selected. The garnet equilibrium formation is pointed in a black square. The brown arrow shows the P–T path of the sample FO1710 suggested by the mineral composition, observed assemblages, and textures.

presence of platy ilmenite aligned in the Se2 foliation, the P–T of 7 kbar/540°C may be indicative for the Se2–Fe2 ductile structure as a whole.

The calculated white mica composition at 7 kbar/540°C is characterized by a Si content of 3.06 Si pfu (Figure 11E). This corresponds to a low Si cluster of the analyzed mica grains being in equilibrium with the garnet. Higher Si contents up to 3.18 Si pfu in white mica must therefore have been crystallized at either high pressure or lower temperature or a combination of both. Previous higher P conditions are not very probable because no indication for Ca rich garnet cores has been found (Figure 11C). A more reliable interpretation is that high-Si white mica represents an earlier, subgreenschist facies generation that has not been erased during prograde evolution (Figure 11E).

Such conditions in the range of 5–7 kbar/300°C would imply that titanite was stable instead of ilmenite. Obviously, titanite was completely converted to ilmenite (+garnet) during temperature increase (Figure 10). The late-stage metamorphic evolution is characterized by the formation of thin Mn richer rims in the garnet border pointing to corrosion still in the stability field of the garnet. Later, the replacement of biotite and garnet by chlorite occurred. According to the derived data, the most probable interpretation is to assume a P–T path characterized by roughly isobaric heating starting at subgreenschist facies conditions up to 7 kbar/540°C (Figure 11H).

5 Discussion

5.1 Origin and tectonic significance of the Zarao Metavolcanic Rocks

5.1.1 Zarao metabasalts

Based on the petrological and geochemical data presented in Section 4.1 and 4.3, the protoliths of the metabasaltic rocks are subalkaline basalts with N-MORB, E-MORB, and P-MORB geochemical affinities (Figures 5B,C). A supra-subduction zone setting of formation of the basaltic protolith is supported by the Nb-Ta negative anomalies of the P-MORB and E-MORB and by the Nb negative anomaly of the N-MORB type metabasalts (Figure 5D). The input of the subdction is also observable in the Th/Yb vs. Nb/Yb diagram, where the P-MORB plot above the MORB-OIB array (Figure 6A, Pearce, 2008). Similar geochemical abundances (Figures 5, 6) are shown by the metabasalt from the Huilma-2 borehole (sample HU2-T5) which is located in the eastern slope of the Coastal Cordillera, next to the garnet-bearing schist of Huilma-1 borehole (>460–400 Ma U-Pb zircon maximum depositional age; Hervé et al., 2018). These features suggest a wider geographical extension of the Zarao Metavolcanic Rocks than what was previously considered by Palape (2020).

The depth of melting for basaltic magma formation can be addressed using the TiO_2/Yb vs. Nb/Yb diagram proposed by Pearce (2008), and it indicates shallow melting for the Zarao metabasalts (Figure 6B). High Sm/Yb_N ratios are related to the influence of garnet on the petrogenesis of basalts (e.g., Kay and Kay, 1991; Kay and Mpodozis, 2001). Willbold and Stracke (2006) compiled geochemical data from ocean island representing the major OIB families and obtained a Sm/Yb_N mean value of 4.79 ± 0.56 among them. The ~1.95 Sm/Yb_N ratio of the P-MORB metabasalts is lower than the average OIB, in agreement with shallower mantle melting in the spinel stability field. The E-MORB and N-MORB have lower Sm/Yb_N ratios of 1.09 and 0.89, respectively. The Ce/Y parameter has been used as a proxy to estimate the Moho depth in arc lavas, and thus the crustal thickness, with lower values related to thinner crust (Mantle and Collins, 2008). The Ce/Y ratios of the Zarao metabasalts vary from 1.42 to 1.48 in the P-MORB, to 0.63 in the E-MORB and toward 0.23 in the N-MORB (Table 1), which supports the formation of these rocks in an environment of thin crust, but of variable thickness (between ~25 and 10 km thick following the work of Mantle and Collins, 2008).

The Sr-Nd-Pb isotope composition of the Zarao Metavolcanic Rocks shows a narrow composition in the $^{207}Pb/^{204}Pb_t$ vs. $^{206}Pb/^{204}Pb_t$ space (Figure 7B) and is similar to the Bulk Silicate Earth (BSE) reservoir of Zindler and Hart (1986), not shown. However, a significative variation in the εNd_t vs. $^{87}Sr/^{86}Sr_t$ and $^{207}Pb/^{204}Pb_t$ vs. $^{208}Pb/^{204}Pb_t$ space is observed among the three types of basaltic protoliths (Figures 7A–C), reflecting a progressive change in the mantle source from an Enriched Mantle 1 (EM1) type toward a Depleted MORB Mantle (DMM) type.

The heterogeneity observed in the geochemistry of the Zarao Metavolcanic Rocks probably reflects different mantle sources and slab fluids involved in the magma generation, which is not uncommon on backarc volcanism environments (e.g., Ducea et al., 2015). Furthermore, we consider that the systematic variations of mantle sources, subduction input, and depth of melting observed in the metabasaltic protoliths may have a diachronic origin. The P-MORBs are derived from an EM-1 like mantle source, have a more marked slab input, and were formed in a relatively thicker crust. The N-MORBs were formed by mantle melting of the DMM-like source, with minor slab influence, and formed in a thin crust setting. Finally, the E-MORB metabasalt is a transitional composition between P-MORB and N-MORB.

5.1.2 Zarao metarhyolites

Despite the high LOI values (5.89 wt%) obtained in the Zarao metarhyolite sample, the geochemical abundance of the less mobile elements is similar to those reported by Rapela et al. (2021), and therefore, the obtained results are useful for the geochemical evaluation (Figure 5). The Zarao metarhyolite has an alkaline geochemical signature as deduced from the MALI value of 10.22 (MALI calculated in wt% as $Na_2O+ K_2O–CaO$; Frost et al., 2001), in agreement with the Nb/Y ratio of 0.51

(Winchester and Floyd, 1977; modified by Pearce, 1996). These geochemical ratios like those of quartz-saturated magmas agree with the preservation of quartz microphenocrysts of the igneous protolith. The ferroan character of the metarhyolite (Fe*= 0.96, Fe* calculated as Fe*= $FeO_t/(FeO_t/MgO)$) is typical of A-type magmas (Frost et al., 2001). Quezada et al. (2018) distinguished the OIB-like (A_1-type) and arc-like (A_2-type) mixed source of the Zarao metarhyolite based on the Y-Nb-Ga geochemical ratios proposed by Eby (1992) to subdivide A-type granitoids.

The marked negative Eu anomaly (Figure 5C) indicates that the fractionation of feldspar played a major role in its petrogenesis. On the other hand, the flat HREE pattern (Sm_N/Yb_N= 1.19) is indicating that the fractionation of garnet and amphibole during its petrogenesis was not significative (Davidson et al., 2012). Negative anomalies of Nb-Ta and Ti in the NMORB-normalized spider diagram (Figure 5D) together with an impoverishment in the content of high field strength elements (HFSEs) are characteristics like those observed by magmas formed in subduction-related environments or derived from the subcontinental lithospheric mantle (more details below).

The Sr-Nd-Pb isotope composition of the Zarao metarhyolite is similar to the P-MORB metabasalts (Figure 7). This unit shows the Sr-isotope composition ($^{87}Sr/^{86}Sr_t$ = 0.7061, Figure 7A) lower that the one obtained for the P-MORB, and probably closer to the original composition of the igneous protolith of the metarhyolite. The $^{207}Pb/^{204}Pb_t$ and $^{208}Pb/^{204}Pb_t$ composition is like the EM1-type mantle source (Figure 7C). Thus, the isotope data strongly suggest a cogenetic link between the P-MORB metabasalts and the metarhyolites, implying that the enriched isotope composition of the metarhyolite is related to the magma source. Rapela et al. (2021) reported the zircon εHf_t and $\delta^{18}O$ isotope compositions of the Zarao metarhyolite showing negative εHf_t values (−5.5 to −1.2), which agree with the result here presented in whole rock εNd_t data, and $\delta^{18}O$ values between and below mantle array (3.9–5.1), the latter supporting nearly the absence of contamination/assimilation of the upper continental crust in its petrogenesis.

While tholeiitic and calc-alkaline magmas can coexist on the same supra-subduction zone settings, a ~2 wt% H_2O content has been proposed as the limit between both magmatic trends (Zimmer et al., 2010). While lower water contents in magmas (<2 wt%) are expected in the tholeiitic series and are characterized by the suppression of early crystallization of magnetite, water-bearing silicates, such as amphibole and biotite, and plagioclase, the opposite occurs within the calc-alkaline series (e.g., Gill, 1981; Grove and Baker, 1984; Grove et al., 2003). The extreme fractionation of a tholeiitic magma following the crystallization of olivine + plagioclase + pyroxene + Fe-Ti oxides could develop the formation of alkaline rhyolites (e.g., Spulber and Rutherford, 1983; Geist et al., 1995; Whitaker et al., 2008), and it seems to be a dominant process in the generation of bimodal magmatism in continental rift-related settings and zones of mantle upwelling (Bachmann and Bergazantz, 2008; Ayelew and Ishiwatari, 2010). The large Eu and Ti negative anomalies displayed by the Zarao metarhyolite agree with the major fractionation of feldspar and Fe-Ti oxides, respectively. According to Spulber and Rutherford (1983), during the fractionation of a tholeiitic magma, plagioclase fractionation is far more relevant under low-pressure conditions, while amphibole fractionation plays a major role at pressures >2 kbar, despite the oxygen fugacity of the magma. Then, it is possible that the magmatic differentiation toward rhyolitic compositions occurred in a magmatic chamber located at shallow crustal depths. Furthermore, the tholeiitic differentiation trend promotes the early crystallization of ^{18}O-enriched mineral phases such as feldspar, instead of ^{18}O-depleted minerals like amphibole or magnetite; thus, extreme fractional crystallization could lead to the formation of an ^{18}O-depleted magma (Taylor, 1968; Gao et al., 2018). While this is a plausible mechanism to explain the low $\delta^{18}O$ values of the Zarao metarhyolite, the assimilation of the high-temperature altered mafic crust cannot be discarded (Troch et al., 2020).

5.1.3 Magmatism during forearc rifting to marginal backarc basin transition

The age of the basaltic protolith of the Zarao Metavolcanic Rocks is shaded by late Carboniferous to Permian tectono-thermal events that affected the metamorphic units in the Coast Range. Duhart et al. (2001) reported K-Ar ages of ca. 297 Ma and 269 Ma for this unit (Figure 2B), and thus, some inferences need to be done to unravel the relative ages among the Zarao metabasalts. As stated in the previous section, the origin of the Zarao metarhyolite is associated with the extreme fractional crystallization of a mafic magma such as the P-MORB metabasalts. Considering that the Zarao metarhyolite was formed from the differentiation of basaltic magmas, it requires that the basalt sources were not solidified yet at the time of magma differentiation, and therefore, it is interpreted that the P-MORB metabasalts and the Zarao metarhyolite are roughly contemporaneous. In this scenario, the geochemical variations observed in the Zarao metabasalt are diagnostic of progressive lithospheric thinning over a supra-subduction zone setting. This tectonic context agrees with the Middle Devonian tectonic evolution proposed by Rapela et al. (2021) for the segment.

Basaltic magma geochemistry can be used as a tectonic setting tracer due to its low fractionation and low degree of crustal contamination (e.g., Pearce, 2014; Xia and Li, 2019). In the Y-La-Nb tectonic discrimination diagram (Cabanis and Lecolle, 1989), the Zarao metabasalts plot mostly in the continental tholeiites and oceanic backarc fields (Figure 6C). These compositional fields are intermediate between the orogenic, arc-related basalt domains (with a

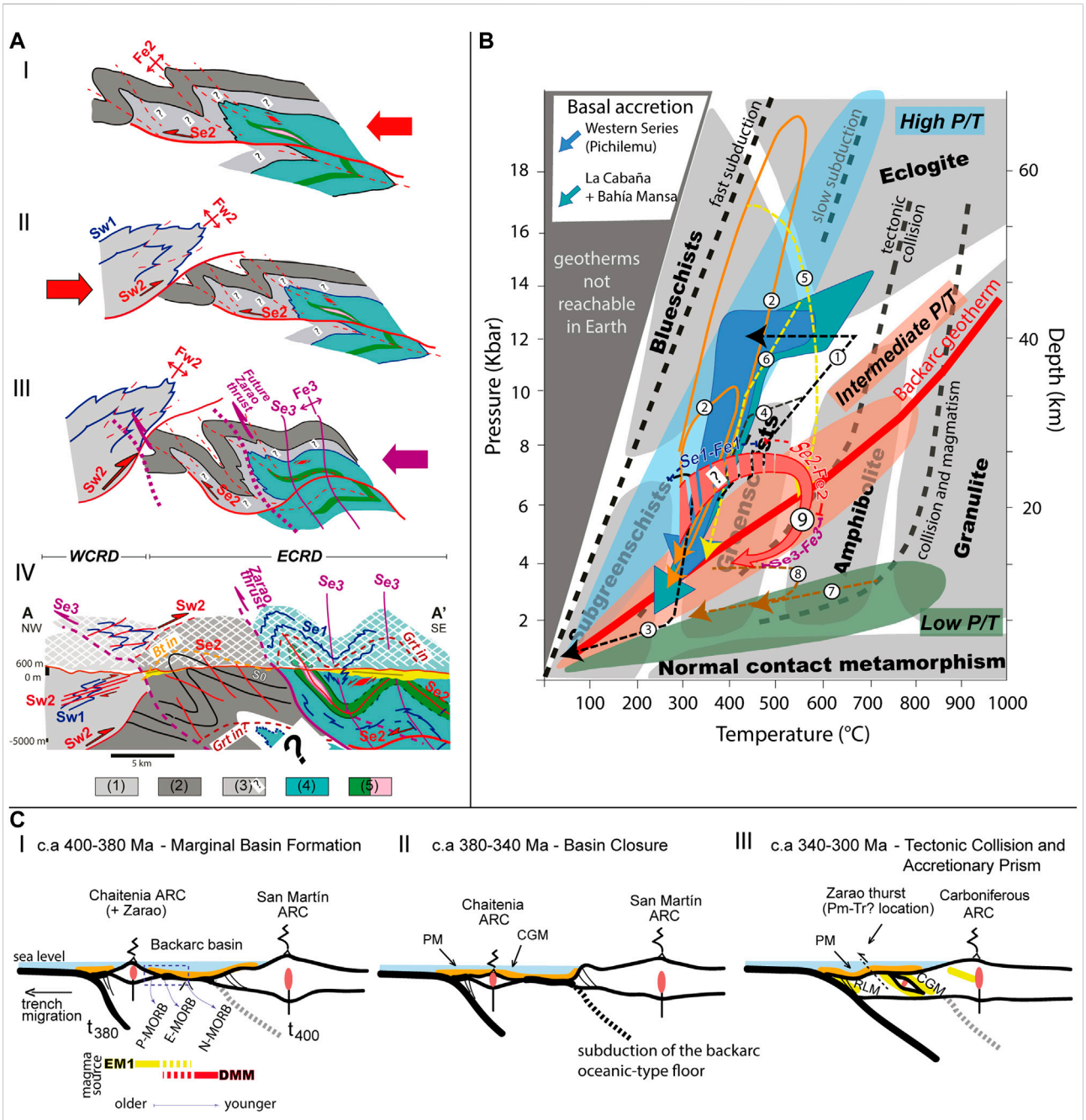

FIGURE 12
Metamorphism, and structural and tectonic analysis. **(A)** Schematic sketch for the development of the structures presented in this study. **(I)** Se2–Fe2 ductile structures, **(II)** Sw2–Fw2 ductile structures, **(III)** Se3–Fe3 ductile structures, and **(IV)** final stage. (1) Río Llico Micaschists, (2) Pinuno Metasandstones, (3) unknown unit, (4) Cajonmo Garnet Micaschists, and (5) Zarao Metavolcanic Rocks. **(B)** Compilation of P–T paths of the Chilean metamorphic basement above the metamorphic facies with geologic geotherm processes modified from the work of Bucher and Grapes (2011). The metamorphic field gradient of the metamorphic series and the backarc geotherm were extracted from the work of Oh (2021) and Hyndman (2019), respectively. The P–T paths are extracted from the work of (1) Willner et al. (2004), (2) Plissart et al. (2021), (3) Willner et al. (2001), (4) Hyppolito et al. (2014), (5) Cruz-Martínez et al. (2012), (6) Kato and Godoy (2008), (7) Willner (2005), (8) Hyppolito et al. (2015), and (9) this work. **(C)** Schematic cross section showing the margin evolution of the Devonian–Carboniferous North Patagonian segment. **(I)** ca. 400–380 Ma: marginal backarc basin formation, **(II)** ca. 380–340 Ma: basin closure, and **(III)** ca. 340–300 Ma: tectonic collision and accretionary prism development. PM: Pinuno Metasandstones, CGM: Cajonmo Garnet Micaschits, and RLM: Río Llico Micaschits.

low La/Nb ratio), and the anorogenic N-MORB/E-MORB/OIB domains (with a high La/Nb ratio). The progression from a continental extensional setting (P-MORB type) toward an oceanic backarc setting (N-MORB type) is in concordance with the crustal thickness changes deduced from the proxies previously used (e.g., Ce/Y, Sm/Yb_N, Section 5.1.1). Thus, it is proposed that the Zarao metabasalts represent the northward prolongation of the Chaitenia marginal basin, the latter previously described in the Reñihue Fjord area (Figure 1A), where a similar geochemical diversity of metabasaltic-types (Figures 5, 6) having a Middle Devonian age crops out (Hervé et al., 2018; Rapela et al., 2021).

Rapela et al. (2021) noted the similar zircon εHf_t values between the calc-alkaline plutons of the San Martin arc (ages between ca. 405 and 395 Ma) and the Zarao metarhyolite (ca. 393 Ma) and suggested that both were formed over the same lithospheric block. The EM-1 like mantle source of the P-MORB metabasalts, combined with their depletion of high field strength elements (HFSEs) such as Nb, Ta, and Ti, suggests that they may have formed by low-pressure partial melting of the metasomatized subcontinental lithospheric mantle (SCLM) (Salters and Shimizu, 1988; O'Reilly and Griffin, 2012). The partial melting was favored by the rollback of the down going slab and adiabatic decompression due to primitive (DMM-type) mantle upwelling, which lead to enhanced extension in the upper plate and the detachment of the forearc away from the waning San Martin arc (Rapela et al., 2021).

As the locus of arc magmatism switched toward the detached forearc, namely, the 'Chaitenia island arc', a spreading center with a typical DMM-like mantle source was progressively stablished in the backarc basin, where the E-MORB and N-MORB Zarao metabasalts were formed. Backarc basin basalts have a mixed tholeiitic geochemical signature between typical N-MORB and arc magmas (Stern, 2010); however, the subduction input in backarc basin basalts will be more subtle as we move away from the volcanic arc front, i.e., toward the more mature portions of the backarc system (e.g., Xia and Li, 2019). This is the case proposed for the Zarao metabasalts, with the E-MORB being formed in early stages of backarc spreading (Nb-Ta anomaly plus a mantle source transitional between EM-1 and DMM), and the N-MORB metabasalts formed during more mature stages (an Nb anomaly and a DMM source). However, we acknowledge that these tectonic processes are complex and other interpretations may be suitable as well.

Coeval with the initial stages of forearc extension and the formation of the Zarao metarhyolite, the Caleta Gonzalo diorite was formed near Reñihue (392 ± 3 Ma, Figure 1A). It corresponds to the older calc-alkaline intrusive of the Chaitenia oceanic arc (Rapela et al., 2021). The REE abundances of this diorite are characterized by a "spoon-shaped" REE pattern indicative of amphibole fractionation (Figure 5) (Davidson et al., 2012). The zircon O-Hf isotope composition is marked by low $\delta^{18}O$ values (+3.8 to +4.5) like those shown by plagiogranites intruding supra-subduction zone ophiolites (Grimes et al., 2013), and highly primitive εHf_t values (14.8–16.7) indicating derivation from a depleted mantle source (Rapela et al., 2021), as it was observed in the N-MORB Zarao metabasalts. The north-south mantle source variations between the Zarao area (enriched mantle) and the Reñihue area (depleted mantle) may be indicating diachronism in the opening of the backarc basin; while the Zarao area was at an embryonic stage of continental thinning, the Reñihue area seafloor spreading in the backarc was already active at ca. 393 Ma. Further north, at the La Cabaña area (Figure 1A), ultramafic rocks have been interpreted to be formed in an oceanic backarc setting (González-Jiménez et al., 2014). This unit is related to schists having youngest detrital zircon age peaks between ca. 352 and 341 Ma (Romero et al., 2018). Speculatively, the spatial and temporal relationships observed along the strike of the Chaitenia arc/backarc system might be indicative of backarc basin opening from south to north.

5.2 Deformation recorded in the metamorphic basement and their relationship with the tectonic events

The Devonian to early Carboniferous rocks of the Eastern and the Western Coastal Range Domain were affected by the superposition of different deformational events. Five structures of ductile deformation were identified, three in the Eastern Coastal Range Domain and two in the Western Coastal Range Domain, Se1–Fe1, Se2–Fe2, and Se3–Fe3, and Sw1–Fw1, Sw2–Fw2, respectively. The Se2–Fe2 ductile structure of the Cajonmo Garnet Micaschists as described in Section 4.2.2 is composed by a detached Fe2 tight fold whose axial plane Se2 foliation is anastomosed developing sigmoidal quartz bands and white micas. These structural features are associated with non-coaxial deformation occurring in the proximities of the Se2 basal thrust responsible of the formation and the detachment of the Fe2 fold (Figures 12A,I). Furthermore, the fold recognized in the Pinuno Metasandstones has the same vergence of the Se2–Fe2 ductile structure (Figures 2C, 12A,I). Hence, we propose that the axial plane foliation of the Pinuno Metasandstones is related to this major structure developed in a shallower structural level as a propagation from its selves (Figures 12A,I). However, the possibility of the Pinuno Metasandstone axial plane foliation related to the Fe1 is not discarded. For the reasons proposed above, Se1–Fe1 and Se2–Fe2 may be related to a progressive deformation, as shown by Fossen et al. (2019), because both ductile structures have rootless isoclinal to tight folds showing similar deformation styles, despite the Se1–Fe1 unknown vergence.

The Fw1 and Fw2 structures observed in the Río Llico Micaschists of the Western Coastal Range Domain were separated from the structures of the Eastern Coastal Range Domain due to differences in the vergence, the spacing of the foliation, the deformational style, and the protolith age. Furthermore, the younger detrital zircons recorded in the Western Coastal Range Domain are Carboniferous, while the younger detrital zircons in the Eastern Coastal Range Domain are Devonian (Hervé et al., 2016; 2018). The Río Llico Micaschists are related to a basally accreted duplex formed in the subduction channel as proposed for the high-pressure metamorphic complexes (Plissart et al., 2021), where the S1 and the S2 metamorphic minerals are dated with $^{39}Ar/^{40}Ar$ *in situ* at ca. 320 Ma and 280 Ma, respectively.

Finally, the Fe3 deformational event is related to west-vergent antiforms and synforms of shorter wavelength, which fold the previous structures of both domains. In the Eastern Coastal Range Domain, the Se3 crenulation is well developed and the Fe3 structures fold the garnet and biotite isograds. However, this deformation does not develop metamorphic minerals. This event culminates with the Zarao thrust, consisting in a brittle structure that thrusted the older Zarao Metavolcanic Rocks surrounded by the Cajonmo Garnet Micaschists above the Pinuno Metasandstones to the WNW (Figures 12,III). Later, a reverse fault took place in the limit between the western and eastern domains related to the Zarao thrust event, where the Pinuno Metasandstones rise above the Río Llico Micaschist (Figures 12,IV). Based on the contact relationships, the Fe3 structures of ductile–brittle deformation are the last compressive folding-fault structures, probably developed during the late Permian to Triassic (Duhart et al., 2001). In addition, it is not discarded that the NNE-SSW Zarao thrust trace has more persistence to the NNE. This considers the residual gravity anomaly that shows a prolongation to the NNE trend lineament of contrasting gravity units below the Cenozoic sedimentary deposits (Yañez & Rivera, 2019), which implies the possibility of the extension of this reverse fault.

5.3 P-T-D metamorphic path during Chaitenia backarc closure

Based on the growth relationships of mineral phases during the structures of ductile deformation complemented with the thermodynamic modelling, summarized in Figures 8–11, a P–T path was determined for the Cajonmo Garnet Micaschist, which is considered to represent the backarc basin closure (Figure 12B). Taking the crystallization and deformation relationships of the FO1710 sample, it is extracted that the Se1–Fe1 and Se2–Fe2 ductile structures are related to burial heating following isobaric heating and isothermal decompression, respectively (Figure 11).

The prograde path was constrained using the white mica with the highest Si content and suggests that the prograde path is related to the burial heating metamorphism. This metamorphism is associated with Fe1 isoclinal folds and is developed from lower pressures and temperatures to reach P–T conditions of ~5 kbar and 300°C, which yields subgreenschist facies. Similarly, the highest Si content in white mica suggest an isobaric thermal path for the Se1–Fe1 ductile structure at ~7 kbar and 400°C–540°C.Using mineral equilibria between oligoclase + garnet + ilmenite + low 3.06 Si in the white mica cluster (cf. Section 4.4.2), it is inferred that the mineral phases reached a metamorphic peak in the garnet zone, which yield amphibolite facies during the Se2–Fe2 ductile structure. Therefore, the isothermal decompression path during the Se2–Fe2 ductile structure is followed by the post-tectonic garnet crystallization, reaching ~5 kbar and 550°C. The similarity in P-T conditions of garnet #1 rim to garnet #2 suggests the retrograde path is linked to almost isothermal decompression and can be related to the detached Fe2 isoclinal by the Se2 basal thrusting (Figures 12A,I). Following the retrograde event, the P–T path follows a decompression with cooling at ~4 kbar and 400°C, which was constrained from the intersection of the retrograde chlorites (Figure 11E) and lower Si content in white mica (Figure 11H). We relate this event to the Se3–Fe3 ductile structures, which do not develop metamorphic mineralogy. Finally, the Zarao thrust continued the decompression with cooling in brittle conditions from ~4 kbar to 400°C to the surface.

The P–T path obtained in this work differs from those presented along the Paleozoic metamorphic basement between ~34° and 40°S, where the metamorphism yields relatively high gradients in the Eastern Series (Figure 12B; Willner, 2005; Hyppolito et al., 2015). When the P–T path here obtained is compared with the gradients presented by Bucher and Grapes (2011), it suggests that the prograde gradient of the Cajonmo Garnet Micaschist is associated with slow subduction and the retrograde gradient coincides with tectonic collision. Furthermore, when it is compared to a global gradient compilation (Oh, 2021), the Cajonmo Garnet Micaschist gradient is mainly intermediate P/T to low P/T, which follows a Barrovian path. Such a gradient has also been found to be related to backarc basin closure (Hyndman, 2019). Finally, it is noteworthy that the basin closure, which is represented in Cajonmo Garnet Micaschists, may have amalgamated in a few meters several metavolcanic rocks of different sources, such as P-MORB, N-MORB, etc.

5.4 Tectonic evolution

The Devonian to Carboniferous tectonic evolution of the studied segment of southwestern Gondwana is dominated by accretionary orogenesis dynamics and can be comprised in three

tectonic stages. The first stage occurred during 400 and 380 Ma and consists in the rifting of the forearc region from the Early-Middle Devonian San Martin continental arc in the Argentinian North Patagonian Andes (Figures 12C,I). This may have been triggered by roll-back dynamics which allowed the beginning of the marginal extensional basin in the margin of Gondwana (Rapela et al., 2021). During this stage, the Zarao metavolcanic rocks were formed with P-MORB signatures during early forearc rifting stages, and the E-MORB signatures developed in the early backarc basin expansion center. The backarc basin was fully developed by the time when the Zarao Metavolcanic Rocks yield N-MORB signature formation. This volcanism occurred in the expansion center located in an inland position with respect to the Chaitenia Island Arc (Hervé et al., 2016). After ~15 Ma, the expansion center of the backarc basin ceased the spreading (Rapela et al., 2021).

The second stage comprises the onset of the backarc basin closure, concomitant with a second subduction zone activated in the western edge of the North Patagonian Massif between ca. 380 and 340 Ma (Hervé et al., 2018) (Figures 12C,I). The forearc and the backarc basins of the Chaitenia Island Arc were covered by the sedimentary strata, which are the protolith of the Pinuno Metasandstones and Cajonmo Garnet Micaschists.

The third stage consists in the metamorphism generated by the collision of the Chaitenia island arc with the North Patagonian Massif ca. 340 and 300 Ma (Hervé et al., 2018; Rapela et al., 2021) (Figures 12C,I). The collision amalgamated and buried a part of the Chaitenia Island Arc with the Zarao Metavolcanic Rocks and the Cajonmo Garnet Micaschists against the North Patagonian Massif. This process is recorded in the Cajonmo Garnet Micaschist, where the Se1–Fe1 ductile structure was produced by the burial and heating the Cajonmo sediments at depths of ~17 km with 300°C, which is accompanied by the Zarao Metavolcanic Rocks along with the Chaitenia Island Arc. This structure was followed by the Se2–Fe2 ductile structure, which corresponds to the isobaric heating at ~25 km and a temperature of 540°C, yielding a metamorphic gradient that is not commonly related to a tectonic collision path. We interpret that the retrograde decompression is related to the west-vergence Fe3 cylindric chevron folds at ~13 km and 450°C. Based on the prolongation to the south of the Carboniferous accretionary prism (Plissart et al., 2021), it is probable that the Río Llico Micaschists developed after the Chaitenia collision in a basally accretionary prism under HP–LT conditions. The final exhumation of the Cajonmo Garnet Micaschist is attributed to the west-vergent Zarao thrust. This process raised these units above the almost undeformed Pinuno Metasandstones, probably toward the Permian and Triassic (Duhart et al., 2001).

6 Conclusion

The geological processes involved in the Devonian accretionary orogen of North Patagonia (Rapela et al., 2021) represents a complete cycle of accretionary orogenesis (e.g., Cawood et al., 2009). Furthermore, the Bahía Mansa Metamorphic Complex has been here separated in two domains, which yield a different protolith, geochemistry, structure, metamorphism, and age. Furthermore, they have distinct tectonic evolutions along the Devonian to Permian accretionary orogen of southwestern Gondwanan margin. Three tectonic stages have been identified: 1) ca. 400–380 Ma rifting of the forearc development of a backarc marginal basin accompanied with sedimentation, 2) ca. 380 and 350 Ma backarc basin closure, and 3) ca. 340 and 300 Ma collision of the forearc and Chaitenia island arc against the southwestern Gondwana margin followed by its exhumation, which resulted in the regional metamorphism.

The geochemistry and the isotopic data of the Zarao Metavolcanic Rocks allow us to infer a magmatic evolution. They are related to a spreading oceanic floor in a suprasubduction condition with P-MORB affinity in the early stage of the development of a marginal basin. This was probably produced by a roll-back event present in the margin of southwestern Gondwana. This volcanism in the marginal basin progressively evolved toward E-MORB magmas and eventually to N-MORB magmas when the marginal basin achieved a mature backarc stage.

Thermodynamic studies conducted in the metasediments of the Eastern Coastal Range Domain record an IP–IT clockwise P–T Barrovian collisional path associated with the collision of the forearc and Chaitenia island arc against the margin. The metamorphism reached a peak of ~25 km at 540°C, following an isothermal decompression of ~13 km at 450°C.

The final exhumation of these metasediments was related to basally accretion in the prism after collision during the Carboniferous to early Permian. Finally, these rocks were affected by brittle deformation in a shallow crust position along the Zarao thrust during the Permian-Triassic.

Data availability statement

The original contributions presented in the study are included in the article/Supplementary Material; further inquiries can be directed to the corresponding author.

Author contributions

CP: writing—original draft, conceptualization, methodology, formal analysis, investigation, and

visualization. PQ: writing—review and editing, conceptualization, methodology, formal analysis, data curation, investigation, and visualization. JB: funding acquisition, validation, writing—review and editing, supervision, investigation, data curation, and resources. FH: conceptualization, funding acquisition, writing—review and editing, supervision, investigation, resources, and project administration. TR: investigation and visualization. MV: investigation. FV: investigation. MC: investigation, visualization, supervision, and project administration. TT: data curation, software, validation, and formal analysis. FF: investigation. MC: data curation, validation, and formal analysis.

Funding

The projects Fondecyt 1130227 and 1180457 financed the research and field campaigns. JB was funded by the Instituto Antártico Chileno (INACH, project RT-06–14) and the Swiss National Science Foundation (project P500PN_202847).

Acknowledgments

We thank Christian Creixell for editorial handling and are grateful to Sebastián Oriolo and a reviewer, who along with the editor, provided constructive criticism that improved the manuscript.

Conflict of interest

The authors declare that the research was conducted in the absence of any commercial or financial relationships that could be construed as a potential conflict of interest.

Publisher's note

References

Aguirre, L., Hervé, F., and Godoy, E. (1972). Distribution of metamorphic facies in Chile, an outline. *Krystalinikum* 9, 7–19.

Angì, G., Cirrincione, R., Fazio, E., Fiannacca, P., Ortolano, G., Pezzino, A., et al. (2010). Metamorphic evolution of preserved hercynian crustal section in the serre Massif (Calabria-Peloritani orogen, southern Italy). *Lithos* 115, 237–262. doi:10.1016/j.lithos.2009.12.008

Ayalew, D., and Ishiwatari, A. (2010). Comparison of rhyolites from continental rift, continental arc and oceanic island arc: Implication for the mechanism of silicic magma generation. *Isl. Arc* 20 (1), 78–93. doi:10.1111/j.1440-1738.2010.00746.x

Bachmann, O., and Bergantz, G. W. (2008). Rhyolites and their source mushes across tectonic settings. *J. Petrology* 49, 2277–2285. doi:10.1093/petrology/egn068

Bahlburg, H. (2021). A Silurian-Devonian active margin in the proto-Andes – new data on an old conundrum. *Int. Geol. Rev.* 2021, 1–22. doi:10.1080/00206814.2021.2012719

Bahlburg, H., and Hervé, F. (1997). Geodynamic evolution and tectonostratigraphic terranes of northwestern Argentina and northern Chile. *Geol. Soc. Am. Bull.* 109, 869–884. doi:10.1130/0016-7606(1997)109<0869:geatto>2.3.co;2

Baker, J., Peate, D., Waight, T., and Meyzen, C. (2004). Pb isotopic analysis of standards and samples using a 207Pb/204Pb double spike and thallium to correct for mass bias with a double-focusing MC-ICP-MS. *Chem. Geol.* 211, 275–303. doi:10.1016/j.chemgeo.2004.06.030

Béguelin, P., Chiaradia, M., Beate, B., and Spikings, R. (2015). The Yanaurcu volcano (Western Cordillera, Ecuador): A field, petrographic, geochemical, isotopic and geochronological study. *Lithos* 218, 37–53. doi:10.1016/j.lithos.2015.01.014

Bell, A. M. (1981). Vergence: an evaluation. *J. Struct. Geol.* 3 (3), 197–202.

Bell, T. H., and Johnson, S. E. (1992). Shear sense: A new approach that resolves problems between criteria in metamorphic rocks. *J. Metamorph. Geol.* 10, 99–124. doi:10.1111/j.1525-1314.1992.tb00074.x

Bernhardt, H. J., Massonne, H. J., Reinecke, T., Reinhardt, J., and Willner, A. (1995). Digital element distribution maps, an aid for petrological investigations. *[Berichte der Deutschen Mineralogischen Gesellschaft] Beihefte zum Eur. J. Mineralogy* 7 (1), 28.

Boedo, F. L., Pérez Luján, S., Ariza, J. P., and Vujovich, G. I. (2021). The mafic-ultramafic belt of the Argentine precordillera: A geological synthesis. *J. S. Am. Earth Sci.* 110, 103354. doi:10.1016/j.jsames.2021.103354

Boynton, W. V. (1984). "Cosmochemistry of the rare earth elements: meteorite studies," in *Developments in Geochemistry* (Elsevier), Vol. 2, 63–114.

Brandelik, A. (2009). CALCMIN–an EXCEL™ Visual Basic application for calculating mineral structural formulae from electron microprobe analyses. *Comput. Geosciences* 35 (7), 1540–1551. doi:10.1016/j.cageo.2008.09.011

Brown, M. (2007). Metamorphism, plate tectonics, and the supercontinent cycle. *Earth Sci. Front.* 14, 1–18. doi:10.1016/s1872-5791(07)60001-3

Bucher, K., and Grapes, R. (2011). *Petrogenesis of metamorphic rocks*. Berlin, Heidelberg: Springer-Verlag. doi:10.1007/978-3-540-74169-5_9

Cabanis, B. V., and Lecolle, M. (1989). Le diagramme La/10-Y/15-Nb/8 un outil pour la discrimination des series volcaniques et la mise en evidence des processus de mélange et/ou de contamination crustale. *Comptes Rendus l'Academie Sci. Ser. II* 309, 2023–2029.

Calderón, M., Massonne, H. J., Hervé, F., and Theye, T. (2017). P–T–time evolution of the mejillones metamorphic complex: Insights into late triassic to early jurassic orogenic processes in northern Chile. *Tectonophysics* 717, 383–398. doi:10.1016/j.tecto.2017.08.013

Campos, A., Moreno, H., Muñoz, J., Antinao, J., Clayton, J., and Martin, M. (1998). *Área de Futrono-Lago Ranco*. Santiago: Servicio Nacional de Geología y Minería, Mapas Geológicos, No. 8, 1 mapa escala 1:100.000.

Cawood, P. A., Kröner, A., Collins, W. J., Kusky, T. M., Mooney, W. D., and Windley, B. F. (2009). "Accretionary orogens through Earth history," in *Earth accretionary systems in space and time. Geol. Soc. Lond. Spec. Publ.* Editors P. A. Cawood and A. Kröner, 318, 1–36. doi:10.1144/SP318.1

Chiaradia, M. (2015). Crustal thickness control on Sr/Y signatures of recent arc magmas: An Earth scale perspective. *Sci. Rep.* 5, 8115. doi:10.1038/srep08115

Chiaradia, M., Müntener, O., and Beate, B. (2011). Enriched basaltic andesites from mid-crustal fractional crystallization, recharge, and assimilation (Pilavo Volcano, Western Cordillera of Ecuador). *J. Pet.* 52, 1107–1141. doi:10.1093/petrology/egr020

Collins, W. J. (2002). Hot orogens, tectonics witching, and creation of continental crust. *Geol.* 30, 535. doi:10.1130/0091-7613(2002)030<0535:hotsac>2.0.co;2

Connolly, J. A. D. (2005). Computation of phase equilibria by linear programming: A tool for geodynamic modeling and its application to subduction zone decarbonation. *Earth Planet. Sci. Lett.* 236, 524–541. doi:10.1016/j.epsl.2005.04.033

Connolly, J. A. D. (1990). Multivariable phase diagrams; an algorithm based on generalized thermodynamics. *Am. J. Sci.* 290, 666–718. doi:10.2475/ajs.290.6.666

Creixell, R., Sepúlveda, F., Álvarez, J., Vásquez, P., and Velásquez, R. (2021). The carboniferous onset of subduction at SW Gondwana revisited: Sedimentation and deformation processes along the late Paleozoic forearc of North Chile (21◦–33◦ S). *J. South Am. Earth Sci.* 107, 103149. doi:10.1016/j.jsames.2020.103149

Crignola, P., Duhart, P., McDonough, M., and Muñoz, J. (1997). Antecedentes geoquímicos acerca del origen de los esquistos máficos y cuerpos ultramáficos en la Cordillera de la Costa, sector norte de la Xa Región, Chile. *Congr. Geol. Chil.* 2 (8), 1254–1258.

Cruz-Martínez, J., Dristas, J. A., and Massonne, H. J. (2012). Palaeozoic accretion of the microcontinent Chilenia, North Patagonian Andes: High-pressure metamorphism and subsequent thermal relaxation. *Int. Geol. Rev.* 54, 472–490. doi:10.1080/00206814.2011.569411

Dahlquist, J. A., Cámera, M. M. M., Alasino, P. H., Pankhurst, R. J., Basei, M. A., Rapela, C. W., et al. (2021). A review of Devonian–Carboniferous magmatism in the central region of Argentina, pre-Andean margin of SW Gondwana. *Earth-Science Rev.* 221, 103781. doi:10.1016/j.earscirev.2021.103781

Dalziel, I. W. D. (1981). Back-arc extension in the southern Andes: A review and critical reappraisal. *Phil. Trans. R. Soc. A* 300, 319–355.

Davidson, J., Turner, S., and Plank, T. (2012). Dy/Dy*: Variations arising from mantle sources and petrogenetic processes. *J. Petrology* 54, 525–537. doi:10.1093/petrology/egs076

Deckart, K., Hervé, F., Fanning, C. M., Ramírez, V., and Calderón, M. (2014). U-Pb geochronology and Hf-O isotopes of zircons from the Pennsylvanian Coastal Batholith, south-central Chile. *Andean Geol.* 41, 49. doi:10.5027/andgeoV41n1-a03

Deng, H., Peng, S., Polat, A., Kusky, T., Jiang, X., Han, Q., et al. (2017). Neoproterozoic IAT intrusion into mesoproterozoic MOR miaowan ophiolite, yangtze craton: Evidence for evolving tectonic settings. *Precambrian Res.* 289, 75–94. doi:10.1016/j.precamres.2016.12.003

Ducea, M. N., Saleeby, J. B., and Bergantz, G. (2015). The architecture, chemistry, and evolution of continental magmatic arcs. *Annu. Rev. Earth Planet. Sci.* 43, 299–331. doi:10.1146/annurev-earth-060614-105049

Duhart, P. (1999). *Geología del Basamento Metamórfico de la Cordillera de la Costa entre los 41°00'- 42°00' L.S., Xa Región, Chile: Consideraciones Geocronológicas*. Chile: Universidad de Concepción, Departamento de Ciencias de la Tierra, 158. Memoria de Título (Unpublished).

Duhart, P., Martin, M., Muñoz, J., Crignola, P., and McDonough, M. (1997). Acerca de la edad del protolito del basamento metamórfico de la Cordillera de la Costa de la Xª Región: Edades preliminares 207Pb/206Pb en circones detríticos. *Congr. Geol. Chil.* 2(8), 1267–1270.

Duhart, P., Mc Donough, M., Muñoz, J., Martin, M., and Villeneuve, M. (2001). El complejo metamórfico Bahía Mansa en la Cordillera de la Costa del centro-sur de Chile (39°30′–42°S): Geocronología K\Ar, 40Ar/39Ar y U\Pb, implicancias en la evolución del margen sur-Occidental de Gondwana. *Rev. Geol. Chile* 28, 179–208. doi:10.5027/andgeoV28n2-a03

Eby, G. N. (1992). Chemical subdivision of the A-type granitoids - petrogenetic and tectonic implications. *Geol.* 20, 641. doi:10.1130/0091-7613(1992)020<0641:csotat>2.3.co;2

Elgueta, S., McDonough, M., Le Roux, J., Urqueta, E., and Duhart, P. (2000). *Estratigrafía y Sedimentología de las Cuencas Terciarias, Región de Los Lagos (39-42° S)*. Chile: Servicio Nacional de Geología y Minería, Boletín 57, 52.

Fortey, R., Pankhurst, R. J., and Hervé, F. (1992). Devonian trilobites at buill, Chile, 42°S. *Rev. Geol. Chile* 19, 133–144.

Fossen, H., Cavalcante, G. C. G., Pinheiro, R. V. L., and Archanjo, C. J. (2019). Deformation–progressive or multiphase?. *J. Struct. Geol.* 125, 82–99.

Frost, B. R., Barnes, C. G., Collins, W. J., Arculus, R. J., Ellis, D. J., Frost, C. D., et al. (2001). A geochemical classification for granitic rocks. *J. Petrology* 42, 2033–2048. doi:10.1093/petrology/42.11.2033

Fuentes, P., Díaz-Alvarado, J., Rodríguez, N., Fernández, C., Breitkreuz, C., Contreras, A. A., et al. (2018). Geochemistry, petrogenesis and tectonic significance of the volcanic rocks of the Las Tortolas Formation, Coastal Cordillera, northern Chile. *J. S. Am. Earth Sci.* 87, 66–86. doi:10.1016/j.jsames.2017.11.006

Gao, Y-Y., Griffin, W. L., Chu, M-F., O'Reilly, S. Y., Pearson, N. J., Li, Q-L., et al. (2018). Constraints from zircon Hf-O-Li isotopic compositions on the Genesis of slightly low-δ18O alkaline granites in the Taohuadao area, Zhejiang Province, SE China. *J. Asian Earth Sci.* 167, 197–208. doi:10.1016/j.jseaes.2017.07.025

Geist, D., Howard, K. A., and Larson, P. (1995). The generation of oceanic rhyolites by crystal fractionation: The basalt-rhyolite association at volc n Alcedo, gal pagos archipelago. *J. Petrology* 36 (4), 965–982. doi:10.1093/petrology/36.4.965

Gianni, G. M., and Luján, S. P. (2021). Geodynamic controls on magmatic arc migration and quiescence. *Earth Sci. Rev.* 2021, 103676.

Gill, J. B. (1981). *Orogenic andesites and plate tectonics*. Berlin: Springer.

Godoy, E., and Kato, T. (1990). Late paleozoic serpentinites and mafic schists from the Coast range accretionary complex, central Chile: Their relation to aeromagnetic anomalies. *Geol. Rundsch.* 79, 121–130. doi:10.1007/BF01830451

González-Bonorino, F. (1970). *Series Metamórficas del Basamento Cristalino de la Cordillera de la Costa de Chile Central*. Chile: Universidad de Chile, Departamento de Geología, Publicación No. 37, 81.

González-Jiménez, J. M., Barra, F., Walker, R., Reich, M., and Gervilla, F. (2014). Geodynamic implications of ophiolitic chromitites in the La Cabaña ultramafic bodies, Central Chile. *Int. Geol. Rev.* 56, 1466–1483. doi:10.1080/00206814.2014.947334

Grimes, C. B., Ushikubo, T., Kozdon, R., and Valley, J. W. (2013). Perspectives on the origin of plagiogranite in ophiolites from oxygen isotopes in zircon. *Lithos* 179, 48–66. doi:10.1016/j.lithos.2013.07.026

Grove, T. L., and Baker, M. B. (1984). Phase-equilibrium controls on the tholeiitic versus calc-alkaline differentiation trends. *J. Geophys. Res.* 89, 3253–3274. doi:10.1029/jb089ib05p03253

Grove, T. L., Elkins-Tanton, L. T., Parman, S. W., Chatterjee, N., Müntener, O., Gaetani, G. A., et al. (2003). Fractional crystallization and mantle-melting controls on calc-alkaline differentiation trends. *Contributions Mineralogy Petrology* 145, 515–533. doi:10.1007/s00410-003-0448-z

Heredia, N., García-Sansegundo, J., Gallastegui, G., Farias, P., Giacosa, R., Alonso, J. L., et al. (2016). Evolución Geodinámica de los Andes argentino-chilenos y la Península Antártica durante el Neoproterozoico tardío y el Paleozoico Late Neoproterozoic-Paleozoic geodynamic evolution of the Argentine-Chilean Andes and the Antarctic Peninsula. *Trab. Geol.* 36, 237. doi:10.17811/tdg.36.2016.237-278

Hervé, F., Calderón, M., Fanning, C. M., Pankhurst, R. J., Fuentes, F., Rapela, C. W., et al. (2016). Devonian magmatism in the accretionary complex of southern Chile. *J. Geol. Soc. Lond.* 173, 587–602. doi:10.1144/jgs2015-163

Hervé, F., Calderón, M., Fanning, C. M., Pankhurst, R. J., and Godoy, E. (2013). Provenance variations in the Late Paleozoic accretionary complex of central Chile as indicated by detrital zircons. *Gondwana Res.* 23, 1122–1135. doi:10.1016/j.gr.2012.06.016

Hervé, F., Calderón, M., Fanning, C. M., Pankhurst, R. J., Rapela, C. W., Quezada, P., et al. (2018). The country rocks of devonian magmatism in the north patagonian Massif and Chaitenia. *Andgeo.* 45 (3), 301. doi:10.5027/andgeoV45n3-3117

Hervé, F. (1988). Late paleozoic subduction and accretion in southern Chile. *Episodes* 11, 183–188. doi:10.18814/epiiugs/1988/v11i3/005

Hervé, F. (1977). *Petrología del basamento cristalino de las montañas Nahuelbuta, centro-sur de Chile*. Chile: Ishikawa T., Aguirre L. Estudios comparativos sobre la geología del cinturón orogénico de Circum Pacific en Japón y Chile. 1–51.

Hervé, M., Suárez, M., and Puig, A. (1984). The Patagonian Batholith S of Tierra del Fuego, Chile: timing and tectonic implications. *J. Geol. Soc.* 141 (5), 909–917.

Hey, M. H. (1954). A new review of the chlorites. *Mineral. Mag. J. Mineral. Soc.* 30, 277–292. doi:10.1180/minmag.1954.030.224.01

Höfer, C., Kraus, S., Miller, H., Alfaro, G., and Barra, F. (2001). Chromite-bearing serpentinite bodies within an arc–backarc metamorphic complex near La Cabaña, south Chilean Coastal Cordillera. *J. S. Am. Earth Sci.* 14, 113–126. doi:10.1016/s0895-9811(01)00011-6

Hofmann, A. W. (2014). "Sampling mantle heterogeneity through oceanic basalts: Isotopes and trace elements," in *Treatise on geochemistry* (Amsterdam, Netherlands: Elsevier), 67–101. doi:10.1016/b978-0-08-095975-7.00203-5

Holland, T. J., and Powell, R. (1998). An internally consistent thermodynamic data set for phases of petrological interest. *J. Metamorph. Geol.* 16, 309–343. doi:10.1111/j.1525-1314.1998.00140.x

Hyndman, R. D. (2019). Origin of regional Barrovian metamorphism in hot backarcs prior to orogeny deformation. *Geochem. Geophys. Geosyst.* 20, 460–469. doi:10.1029/2018GC007650

Hyppolito, T., Garcia-Casco, A., Juliani, C., Meira, V. T., and Hall, C. (2014). Late Paleozoic onset of subduction and exhumation at the Western margin of Gondwana (Chilenia Terrane): Counterclockwise P–T paths and timing of metamorphism of deep-seated garnet–mica schist and amphibolite of Punta Sirena, Coastal Accretionary Complex, central Chile (34° S). *Lithos* 216–217, 409–434. doi:10.1016/j.lithos.2014.07.023

Hyppolito, T., Juliani, C., Garcia-Casco, A., Meira, V. T., Bustamante, A., Hall, C., et al. (2015). LP/HT metamorphism as a temporal marker of change of deformation

style within the Late Palaeozoic accretionary wedge of central Chile. *J. Metamorph. Geol.* 33, 1003–1024. doi:10.1111/jmg.12166

Jackson, S. E. (2008). "LAMTRACE data reduction software for LA-ICP-MS," in *Laser ablation ICP-ms in the earth sciences: Current practices and outstanding issues* (Vancouver, BC, Canada: Mineralogical Association of Canada), Vol. 40, 305–307.

Kato, T., and Godoy, E. (1995). Petrogenesis and tectonic significance of Late Paleozoic coarse-crystalline blueschist and amphibolite boulders in the coastal range of Chile. *Int. Geol. Rev.* 37, 992–1006. doi:10.1080/00206819509465437

Kato, T. T., Sharp, W., and Godoy, E. (2008). Inception of a devonian subduction zone along the southwestern Gondwana margin: ^{40}Ar–^{39}Ar dating of eclogite–amphibolite assemblages in blueschist boulders from the coastal range of Chile (41°S). *Can. J. Earth Sci.* 45, 337–351. doi:10.1139/E08-006

Kay, R. W., and Mahlburg-Kay, S. (1991). Creation and destruction of lower continental crust. *Geol. Rundsch.* 80 (2), 259–278. doi:10.1007/bf01829365

Kay, S. M., and Mpodozis, C. (2001). *Central Andean ore deposits linked to evolving shallow subduction systems and thickening crust*.

Maksymowicz, A., Montecinos-Cuadros, D., Díaz, D., Segovia, M. J., and Reyes, T. (2022). Forearc density structure of the overriding plate in the northern area of the giant 1960 Valdivia earthquake. *Solid earth.* 13, 117–136. doi:10.5194/se-13-117-2022

Mantle, G. W., and Collins, W. J. (2008). Quantifying crustal thickness variations in evolving orogens: Correlation between arc basalt composition and Moho depth. *Geol.* 36, 87. doi:10.1130/G24095A.1

Martin, M., Kato, T., Rodríguez, C., Godoy, E., Duhart, P., McDonough, M., et al. (1999). Evolution of the late Paleozoic accretionary complex and overlying forearc-magmatic arc, south central Chile (38°-41°S): Constraints for the tectonic setting along the southwestern margin of Gondwana. *Tectonics* 18 (4), 582–605. doi:10.1029/1999TC900021

Massonne, H. J., and Calderón, M. (2008). Evolucion P-T de metapelitas del Complejo Guarguaraz, Argentina: Evidencia para el engrosamiento cortical devonico en cercanias del margen Occidental de Gondwana.P-T evolution of metapelites from the guarguaraz complex, Argentina: Evidence for devonian crustal thickening close to the Western Gondwana margin. *Andgeo.* 35 (2), 215–231. doi:10.5027/andgeoV35n2-a02

McArthur, J. M., Howarth, R. J., and Shields, G. A. (2012). "Strontium isotope stratigraphy," in *A geologic time scale*. Editors F. M. Gredstein, J. G. Ogg, M. D. Schmotz, and G. M. Ogg (Amsterdam: Elsevier), 127–144. doi:10.1016/b978-0-444-59425-9.00007-x

McClay, K. R. (1987). *The mapping of geological structures*. London: Geological Society of London Handbook, vi–161.

Molnar, P., and Atwater, T. (1978). Interarc spreading and Cordilleran tectonics as alternates related to the age of subducted oceanic lithosphere. *Earth Planet. Sci. Lett.* 41, 330–340. doi:10.1016/0012-821X(78)90187-5

Muñoz-Montecinos, J., Angiboust, S., Cambeses, A., and García-Casco, A. (2020). Multiple veining in a paleo–accretionary wedge: The metamorphic rock record of prograde dehydration and transient high pore-fluid pressures along the subduction interface (Western Series, central Chile). *Geosph. (Boulder).* 16 (X), 765–786. doi:10.1130/GES02227.1

Oh, C. W. (2021). "P-T-t paths," in *Encyclopedia of Geology*. Second Edition (Cambridge, MA, USA: Academic Press), 597–611. doi:10.1016/B978-0-08-102908-4.00163-6

O'Reilly, S. Y., and Griffin, W. L. (2012). "Mantle metasomatism," in *Lecture notes in earth system sciences* (Berlin, Heidelberg: Springer), 471–533. doi:10.1007/978-3-642-28394-9_12

Palape, C. (2020). *Estructura y metamorfismo del Complejo Metamórfico Bahía Mansa y de la unidad metabasitas de Estaquilla, Cordillera de la Costa de Chile Central Sur (41, 1-41, 6° S; 73, 7-73, 8° W)*. Santiago: Universidad de Chile, 124. Graduation Master thesis (Unpublished).

Pankhurst, R. J., Rapela, C. W., Fanning, C. M., and Márquez, M. (2006). Gondwanide continental collision and the origin of Patagonia. *Earth-Science Rev.* 76, 235–257. doi:10.1016/j.earscirev.2006.02.001

Passchier, C. W., and Trouw, R. A. (2005). *Microtectonics*. 2nd Edition. Berlin, Heidelberg: Springer Science & Business Media, 372.

Pearce, J. A. (1996). "A user's guide to basalt discrimination diagrams," in *Trace element geochemistry of volcanic rocks: Applications for massive sulphide exploration. Geological association of Canada, short course notes*. Editor D. A. Wyman, 12, 79–113.

Pearce, J. A. (2008). Geochemical fingerprinting of oceanic basalts with applications to ophiolite classification and the search for Archean oceanic crust. *Lithos* 100, 14–48. doi:10.1016/j.lithos.2007.06.016

Pearce, J. A. (2014). Immobile element fingerprinting of ophiolites. *Elements* 10 (2), 101–108. doi:10.2113/gselements.10.2.101

Pérez Luján, S., Boedo, F., Ariza, J., Vujovich, G., Alvarado, P., Kay, S., et al. (2021). The Cuyano proto-ocean between the Chilenia and Cuyania terranes: Rifting and plume interaction during the Neoproterozoic – early Palaeozoic evolution of the SW Gondwana margin. *Geol. Mag.* 158 (10), 1773–1794. doi:10.1017/S0016756821000303

Pin, C., and Santos-Zalduegui, J. F. (1997). Sequential separation of light-rare-Earth elements, thorium and uranium by miniaturized extraction chromatography: Application to isotopic analyses of silicate rocks. *Anal. Chim. Acta X.* 339, 79–89. doi:10.1016/s0003-2670(96)00499-0

Plissart, G., Moral, J. C., Pavez, C., Rivera, A., and González-JiménezBerger, J. M. J. (2021). "Registros del canal de subducción tardi-paleozoico en el paleo-prisma del centro-sur de Chile: Un enfoque en la evolución tectono-metamórfica de rocas máficas y ultramáficas de alta presión," in *Simposio Actualización de la Geología de Chile - SAGChi 2021*.

Quezada, P. (2015). *Geología del basamento de la Región de Los Lagos, Chile: Evidencias de magmatismo calco alcalino y aportes sedimentarios devónicos*. Santiago: Universidad de Chile, 95. Graduation thesis (Unpublished).

Quezada, P., Vildoso, F., Marambio, C., Palape, C., Hervé, F., Calderón, M., et al. (2018). "Devonian magmatism in the coastal ranges of the Chilean lake district: The Zarao metatrachyte," in *XV congreso geologico Chileno* (Concepción: Actas), 822–824.

Ramos, V. A. (2009). "Anatomy and global context of the Andes: Main geologic features and the andean orogenic cycle," in *Backbone of the americas: Shallow subduction, plateau uplift, and ridge and terrane collision, vol. 204*. Editors S. M. Kay, V. A. Ramos, and W. R. Dickinson (Memoir: The Geological Society of America), 31–65.

Ramos, V. A., Jordan, T. E., Allmendinger, R. W., Kay, S. M., Cortés, J. M., and Palma, M. (1984). Chilenia: Un terreno alóctono en la evolución paleozoica de los Andes centrales. 9o congreso geológico argentino. *Actas* 2, 84–106.

Ramos, V. A., Jordan, T. E., Allmendinger, R. W., Mpodozis, C., Kay, S. M., Cortés, J. M., et al. (1986). Paleozoic terranes of the central Argentine-Chilean Andes. *Tectonics* 5 (6), 855–880. doi:10.1029/tc005i006p00855

Rapela, C. W., Hervé, F., Pankhurst, R. J., Calderón, M., Fanning, C. M., Quezada, P., et al. (2021). The Devonian accretionary orogen of the North Patagonian cordillera. *Gondwana Res.* 96, 1–21. doi:10.1016/j.gr.2021.04.004

Richter, P. P., Ring, U., Willner, A. P., and Leiss, B. (2007). Structural contacts in subduction complexes and their tectonic significance: The Late Palaeozoic coastal accretionary wedge of central Chile. *J. Geol. Soc.* 164, 203–214. doi:10.1144/0016-76492005-181

Romero, R., Barra, F., Leisen, M., Salazar, E., González-Jiménez, J. M., Reich, M., et al. (2020). Sedimentary provenance of the Late Paleozoic metamorphic basement, south-central Chile: Implications for the evolution of the Western margin of Gondwana. *Int. Geol. Rev.* 62 (5), 598–613. doi:10.1080/00206814.2019.1627589

Romero, R., González-Jiménez, J. M., Barra, F., Leisen, M., Garrido, L. N., Talavera, C., et al. (2018). Timing the tectonic mingling of ultramafic rocks and metasediments in the southern section of the coastal accretionary complex of central Chile. *Int. Geol. Rev.* 60 (16), 2031–2045. doi:10.1080/00206814.2017.1402377

Saccani, E., Allahyari, K., and Rahimzadeh, B. (2014). Petrology and geochemistry of mafic magmatic rocks from the Sarve-Abad ophiolites (Kurdistan region, Iran): Evidence for interaction between MORB-type asthenosphere and OIB-type components in the southern Neo-Tethys Ocean. *Tectonophysics* 621, 132–147. doi:10.1016/j.tecto.2014.02.011

Salters, V. J. M., and Shimizu, N. (1988). World-wide occurrence of HFSE-depleted mantle. *Geochimica Cosmochimica Acta* 52, 2177–2182. doi:10.1016/0016-7037(88)90198-6

Schellart, W. P., Chen, Z., Strak, V., Duarte, J. C., and Rosas, F. M. (2019). Pacific subduction control on Asian continental deformation including Tibetan extension and eastward extrusion tectonics. *Nat. Commun.* 10, 4480. doi:10.1038/s41467-019-12337-9

Schellart, W. P. (2008). Subduction zone trench migration: Slab driven or overriding-plate-driven? *Phys. Earth Planet. Interiors* 170 (1-2), 73–88. doi:10.1016/j.pepi.2008.07.040

Spulber, S. D., and Rutherford, M. J. (1983). The origin of rhyolite and plagiogranite in oceanic crust— An experimental study. *J. Petrology* 24, 1–25. doi:10.1093/petrology/24.1.1

Sun, S., and McDonough, W. F. (1989). Chemical and isotopic systematics of oceanic basalts: Implications for mantle composition and processes. *Geol. Soc. Lond. Spec. Publ.* 42, 313–345. doi:10.1144/GSL.SP.1989.042.01.19

Tanaka, T., Togashi, S., Kamioka, H., Amakawa, H., Kagami, H., Hamamoto, T., et al. (2000). JNdi-1: A neodymium isotopic reference in consistency with

LaJolla neodymium. *Chem. Geol.* 168 (3-4), 279–281. doi:10.1016/S0009-2541(00)00198-4

Tašárová, Z. A. (2007). Towards understanding the lithospheric structure of the southern Chilean subduction zone (36°S–42°S) and its role in the gravity field. *Geophys. J. Int.* 170 (3), 995–1014. doi:10.1111/j.1365-246X.2007.03466.x

Taylor, B., and Karner, G. (1983). On the evolution of marginal basins. *Rev. Geophys.* 21, 1727. doi:10.1029/RG021i008p01727

Taylor, B., and Martinez, F. (2003). Back-arc basin basalt systematics. *Earth Planet. Sci. Lett.* 210, 481–497. doi:10.1016/s0012-821x(03)00167-5

Taylor, H. P. (1968). The oxygen isotope geochemistry of igneous rocks. *Contr. Mineral. Pet.* 19 (1), 1–71. doi:10.1007/bf00371729

Tobisch, O. T., and Paterson, S. R. (1988). Analysis and interpretation of composite foliations in areas of progressive deformation. *J. Struct. Geol.* 10 (7), 745–754. doi:10.1016/0191-8141(88)90081-8

Troch, J., Ellis, B. S., Harris, C., Bachmann, O., and Bindeman, I. N. (2020). Low-δ18O silicic magmas on earth: A review. *Earth-Science Rev.* 208, 103299. doi:10.1016/j.earscirev.2020.103299

Vildoso, F. (2017). *Petrología del Basamento Metavolcánico Devónico de la Cordillera del Zarao, Los Muermos , Región de Los Lagos, Chile, Memoria para optar al Título de Geóloga*. Santiago: Universidad Andres Bello, 110. (Unpublished) Carrera de Geología.

Whitaker, M. L., Nekvasil, H., Lindsley, D. H., and McCurry, M. (2008). Can crystallization of olivine tholeiite give rise to potassic rhyolites? An experimental investigation. *Bull. Volcanol.* 70, 417–434. doi:10.1007/s00445-007-0146-1

Whitney, D. L., and Evan, s. B. W. (2010). Abbreviations for names of rock-forming minerals. *Am. Mineralogist* 95 (1), 185–187. doi:10.2138/am.2010.3371

Willbold, M., and Stracke, A. (2006). Trace element composition of mantle end-members: Implications for recycling of oceanic and upper and lower continental crust. *Geochem. Geophys. Geosyst.* 7. doi:10.1029/2005GC001005

Willner, A., Gerdes, A., Massonne, H. J., Schmidt, A., Sudo, M., Thomson, S., et al. (2011). The geodynamics of collision of a microplate (Chilenia) in Devonian times deduced by the pressure–temperature–time evolution within part of a collisional belt (Guarguaraz complex), WArgentina. *Contrib. Mineral. Pet.* 162, 303–327. doi:10.1007/s00410-010-0598-8

Willner, A. P., Glodny, J., Gerya, T. V., Godoy, E., and Massonne, H. J. (2004). A counterclockwise PTt path of high-pressure/low-temperature rocks from the coastal cordillera accretionary complex of South-central Chile: Constraints for the earliest stage of subduction mass flow. *Lithos* 75, 283–310. doi:10.1016/j.lithos.2004.03.002

Willner, A. P., Massonne, H. J., Gerdes, A., Hervé, F., Sudo, M., and Thomson, S. (2009). "The contrasting evolution of collisional and coastal accretionary systems between the latitudes 30°S and 35°S: Evidence for the existence of a Chilenia microplate," in *Actas XII congreso geológico Chileno* (Santiago: Universidad de Chile), S9_099.

Willner, A. P., Pawlig, S., Massonne, H. J., and Hervé, F. (2001). Metamorphic evolution of spessartine quartzites (coticules) in the high pressure/low temperature complex at Bahia Mansa (Coastal Cordillera of Southern Central Chile). *Can. Mineralogist* 39, 1547–1569. doi:10.2113/gscanmin.39.6.1547

Willner, A. (2005). Pressure–temperature evolution of a late palaeozoic paired metamorphic belt in north–Central Chile (34°–35°30′S). *J. Petrology* 46, 1805–1833. doi:10.1093/petrology/egi035

Willner, A., Thomson, S. N., Kröner, A., Wartho, J. A., Wijbrans, J., Hervé, F., et al. (2005). Time markers for the evolution and exhumation history of a late palaeozoic paired metamorphic belt in north–Central Chile (34°–35°30′S). *J. Petrology* 46, 1835–1858. doi:10.1093/petrology/egi036

Winchester, J. A., and Floyd, P. A. (1977). Geochemical discrimination of different magma series and their differentiation products using immobile elements. *Chem. Geol.* 20, 325–343. doi:10.1016/0009-2541(77)90057-2

Xia, L., and Li, X. (2019). Basalt geochemistry as a diagnostic indicator of tectonic setting. *Gondwana Res.* 65, 43–67. doi:10.1016/j.gr.2018.08.006

Yáñez, G., and Rivera, O. (2019). Crustal dense blocks in the fore-arc and arc region of Chilean ranges and their role in the magma ascent and composition: Breaking paradigms in the Andean metallogeny. *J. S. Am. Earth Sci.* 93, 51–66. doi:10.1016/j.jsames.2019.04.006

Zimmer, M. M., Plank, T., Hauri, E. H., Yogodzinski, G. M., Stelling, P., Larsen, J., et al. (2010). The role of water in generating the calc-alkaline trend: New volatile data for aleutian magmas and a new tholeiitic index. *J. Petrology* 51, 2411–2444. doi:10.1093/petrology/egq062

Zindler, A., and Hart, S. (1986). Chemical geodynamics. *Annu. Rev. Earth Planet. Sci.* 14, 493–571. doi:10.1146/annurev.ea.14.050186.002425